TECHNISCHE UNIVERSITÄT WIEN

Master Thesis

Oxidation- and Oxygen Diffusion-Behaviour in Hafnium Based Thin Films analysed with a ToF-SIMS

to obtain the degree

Master of Science (Diplom Ingenieur)

carried out at the

Institute of Chemical Technologies and Analytics

at TU Vienna

under the supervision of

Ao.Univ.Prof. Dr. Herbert Hutter

by

Lena Haager

Matr.-Nr.: 01426561

Vienna, April 2020

This work was supported by Plansee SE, Plansee Composite Materials GmbH, and Oerlikon Balzers, Oerlikon Surface Solutions AG in the framework of the Christian Doppler Laboratory for Surface Engineering of high-performance Components.

Acknowledgements

I want to give big thanks to the people who have supervised me and made the project of my master thesis possible. I especially want to thank my research supervisor Professor Hutter, who always had an open ear when I needed an advice and also Dr. Helmut Riedl and Thomas Glechner, without whom the cooperation with the Christian Doppler Laboratory for Surface Engineering of high-performance Components would not have been possible.

Special thanks go to Professor Hutters research team, Fabian Bohrn, Peter Kügler, Michael Leitzenberger and Anna Bleier, who taught me how to operate the ToF-SIMS, helped me whenever I had questions and spend lots of fun lunch breaks with me.

I am extremely grateful for Dani, my boyfriend, and Resi, my sister, for always being there and cheering me up, if things did not go like expected.

My biggest thanks though go to my parents, Elisabeth and Heinrich, who have always supported me, stood behind me and made it possible for me to study without worrying.

Abstract

The need for new ultra high-temperature coating material, with phase stability and oxidation resistivity over 2000 °C increased rapidly. Especially aviation and power generation industry, where certain high-performance components are exposed to an extreme environment ask for new advances. Because of their uniquely high melting points and their excellent mechanical properties are hafnium based compounds considered to be promising candidates for new high-temperature resistant coating materials.

In this thesis the oxidation and oxygen diffusion behaviour of HfB_2 and HfN thin films were investigated and compared to those of Hf by analysing depth profiles obtained with a Time of Flight Secondary Ion Mass Spectrometer (ToF-SIMS) - an outstanding and unique method for solid surface analysis.

Thin films of Hf, HfB_2 and HfN were deposited by magnetron sputtering and oxidised in a differential thermal analysis (DTA)/-thermo-gravimetric analysis (TGA) system. Depth profiles of both as-deposited and oxidised samples were analysed and additionally compared to cross-section images of the oxidised samples obtained by a Scanning Electron Microscope (SEM).

To determine the oxygen permeability of the respective oxide layer on top of the Hf, HfB_2 and HfN coatings, a previously oxidised sample of each coating material was reheated to the same temperature in an ^{18}O atmosphere and the ^{18}O signal in a ToF-SIMS depth profile before and after the process was compared.

Hf thin films were found to be a lot less resistive than the non-metal hafnium compounds against both oxidation and oxygen diffusion. Moreover, it was determined that HfB_2 and HfN thin films show similar resistivity against oxidation and oxygen diffusion at lower temperatures but at higher temperature HfB_2 outperforms HfN making HfB_2 a potential seminal candidate for protective coatings of highly stressed aeroplane components.

Kurzfassung

Die Nachfrage an neuen Ultrahochtemperatur-Materialbeschichtungen, mit einer Phasenstabilität- und Oxidationsbeständigkeit von über 2000 °C steigt kontinuierlich an, besonders in der Flugfahrt und Kraftwerksindustrie.

Aufgrund ihrer einzigartig hohen Schmelzpunkte und hervorragenden mechanischen Eigenschaften gelten hafniumbasierende Materialien wie HfB_2 und HfN als vielversprechende Kandidaten für neue hochtemperaturbeständige Beschichtungsmaterialien.

In dieser Arbeit wurde das Oxidations- und Sauerstoffdiffusionsverhalten von HfB_2- und HfN-Dünnfilmen untersucht und mit dem von Hf durch die Analyse von Tiefenprofilen verglichen, welche mit Hilfe eines Flugzeit-Sekundärionen-Massenspektrometers (ToF-SIMS) erzeugt wurden. Dieses Vorgehen ist eine herausragende und einzigartige Methode für die Analyse von festen Oberflächen. Es wurden Dünnfilmschichten von Hf, HfB_2 und HfN durch das Magnetron-Sputter Verfahren erzeugt und anschließend mit einer Differenz-Thermoanalyse (DTA)/-thermogravimetrische Analyse (TGA) oxidiert. Zusätzlich wurden die unterschiedlichen Tiefenprofile mit Querschnittsaufnahmen, welche mit einem Rasterelektronenmikroskop (REM) erzeugt wurden, verglichen.

Es wurde festgestellt, dass Hf-Dünnfilme sowohl gegen Oxidation als auch gegen Sauerstoffdiffusion weniger resistent sind als die Hafniumverbindungen. Darüber hinaus wurde festgestellt, dass HfB_2- und HfN-Dünnfilme bei niedrigeren Temperaturen, ähnlich resistent sind, bei höheren Temperaturen jedoch übertrifft HfB_2 HfN, was HfB_2 zu einem potenziellen zukunftsfähigen Kandidaten für die Schutzbeschichtung hochbelasteter Flugzeugkomponenten macht.

Contents

1 Introduction

Already in the 1960s the industry showed interest in high-temperature materials but, because of their great oxidation resistivity, mostly concentrated on ceramics like SiC and Si_3Ni_4. When exposed to high temperature Silicon based materials build a SiO_2 glass layer preventing oxygen from diffusing into the material. This effect works very well up to 1700 °C, but over this temperature and at reduced pressure a gaseous SiO layer is built, which no longer prevents oxidation.[1]

In the last years the need for new ultra high-temperature materials with temperature resistivity over 2000 °C started to increase, especially in the aviation industry. In particular nozzle components, propulsion system compounds and the wind leading edges of aeroplanes need to be resistant to very high temperatures.[2]

Compounds of boron, nitrogen and carbon with transition metals like Hf or Zr offer promising mechanical properties like an extremely high melting point, high oxygen resistivity and high hardness and stiffness, due to a mixture of covalent, ionic and metallic bonds, but especially because of strong covalent bonds between the non-metal and the metal.[3][4]

This thesis focuses on two hafnium based materials, HfB_2 and HfN, as promising application in protective coating.

2 Hafnium Based Materials

Hafnium is part of the group IV transition metals, as well as titanium and zirconium. Naturally six isotopes of hafnium occur, they are shown in table 2.1. Hafnium has an atomic weight of 178,49 u and an atomic number of 72.[5]

Isotope	Abundance (%)
^{174}Hf	0,18
^{176}Hf	5,15
^{177}Hf	18,39
^{178}Hf	27,02
^{179}Hf	13,78
^{180}Hf	35,44

Table 2.1: Natural isotopes of hafnium

Because of their high melting point and high temperature resistivity hafnium compounds with boron, nitrogen and carbon are part of a material class called Ultra High-Temperature Ceramics UHTCs.

2.1 Ultra High-Temperature Ceramics UHTCs

UHTCs offer a range of promising temperature resistant materials. They are defined as ceramics which are stable over 2000 °C with a melting point over 3000 °C.

There are about 300 materials with a melting point over 2000 °C but only a very small number of materials with a melting point over 3000 °C, including several nitrides, carbides and borides of IVB and VB group transition metals (Figure 2.1).

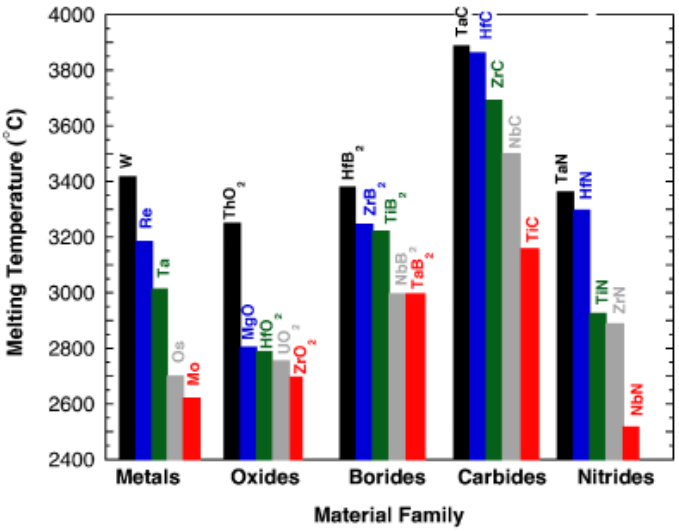

Figure 2.1: Refractory materials with melting points over 2400 °C. Especially nitrides, carbides and borides of IVB and VB group transition metals can have a melting point over 3000 °C.[6]

Since most of the materials used in the aviation industry are exposed to an oxidising environment another important item, besides high temperature resistance, is the oxidation behaviour of the used material. Moreover items like thermal conductivity, thermal expansion, density and cost play an important roll when deciding which material to use. Because of these requirements a lot of UHTCs cannot be considered in the aviation industry. Oxides for example have a bad thermal shock resistivity and some materials like TiC or NbC form low melting oxides. That leaves the industry with mostly hafnium and zirconium based materials (borides, nitrides and carbides), due to their unique properties like outstandingly high melting points and very good resistivity to oxidation up to 2000 °C.[2]

2.2 Hafnium Based Thin Films

In order to support highly exposed components of aeroplanes they have to be coated with a protective film. The structural and mechanical properties though can change if the material is deposited as a thin film (nm - several μm) instead of as a thick ceramic. Thin films are usually obtained from a vapour phase with techniques like Physical Vapour Deposition (PVD)(for further information see chapter 5.1) or Chemical Vapour Deposition (CVD). They often show crystallographic structure with regard to the substrate they are applied onto. Furthermore, when obtaining a thin film, the material becomes denser than a thick ceramic, due to the formation of smaller grains. Also the formation of metastable phases is possible.[7]

2.2.1 Hafniumdiboride Films

Structure and Chemical Bonds

The first material analysed in this thesis is HfB_2. HfB_2 has the structure of the AlB_2 prototype with the boron atoms forming a graphite-like structured layer while the hafnium atoms form a hexagonal closed-packed layer. The two different layers are arranged alternately.[8] (Figure 2.2)

In metalboride-complexes the electronic structure of boron changes depending on the metal to boron ratio, which leads to metalboride-complexes of one-, two- or three-dimensional boron networks. With an increasing number of boron in the complex the B-B strength increases as well. In addition, also the chemical stability, the hardness and the melting temperature increases.

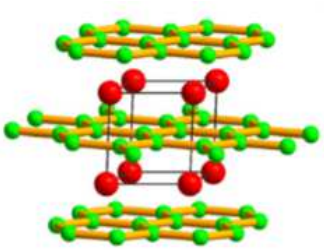

Figure 2.2: Illustration of the crystal structure of HfB_2. (The red dots symbolise hafnium and the green dots symbolise boron)[9]

The metal-boron strength on the other hand depends on the electron delocalisation around the metal. Looking at diborides, the metal functions as an electron donor, donating one electron to each boron atom and the boron atoms function as electron acceptors. That gives the bonds between the metal and the boron atoms an ionic characteristic. On the other hand the valence configuration of borides in metalborides is sp^2 and sp^3 forming spd hybrid configuration due to d excitation which leads to a covalent bond characteristic. [10][11]

Mechanical Properties

Refractory borides show very unique properties like high melting points and hardness as well as a good thermal, corrosion and oxidation resistance. Besides ZrB_2 HfB_2 is the most studied UHTC boride with an outstanding melting point of 3380 °C and a high bulk hardness of 29 GPa.[12]

The hardness of a material depends a lot on the grain size. In general a material is stronger the higher the inverse square root of the grain size is, which indicates that the smaller the grain size is, the higher is the strength.[13]

When HfB_2 is produced as a thick ceramic, the strength can be improved by adding additives. 30 vol% SiC or 30 vol% $MoSi_2$ seems to be working very well when added

to the HfB_2 powder before the sintering process. It increases the density and with it the grain growth slows down and the material becomes stronger. Moreover the flexure strength of HfB_2-SiC and HfB_2-$MoSi_2$ stays the same (550-600 MPa with a grain size of <2 μm) in the range from room temperature to 1500 °C.[14][15]
If HfB_2 is produced as a thin film the mechanical properties are different. The grain size is a lot smaller and therefore very strong films can be produced. Nano crystalline films with up to 40 GPa can be obtained, which makes them much harder than amorphous films (20 GPa) as well as the ceramic bulk hardness (29 GPa).[16]
The Young's modulus of HfB_2 as a thick ceramic is between 445 GPa for pure HfB_2 and 512 GPa for HfB_2 with additives like SiC or $MoSi_2$.[17] Producing a thin film of HfB_2, without additives, the material becomes a little less elastic with an elastic modulus of 430 GPa.[16]

2.2.2 Hafniumnitrid Films

Structure and Chemical Bonds

The second material analysed in this theses is HfN. HfN has the NaCl structure type, if hafnium and nitride have approximately the same at%.(figure 2.3) Beneath a hafnium content of 45 at% respective 29 at% two similar phases, Hf_3N_2 respective Hf_4N_3 are formed, but these structures are unstable over ~2000 °C respectively ~2300 °C. Figure 2.4 shows a precise phase diagram of hafnium and nitrogen.[18]
Like HfB_2 HfN has mixed bond characteristics with both covalent and ionic character.[19] The covalent character of the bonds is higher within HfN than in the bonds of HfB_2. Therefore it is more difficult to form uniformly dens materials, which leads to poorer mechanical properties.[20]

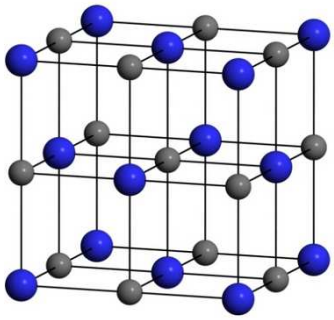

Figure 2.3: Illustration of the crystal structure of HfN

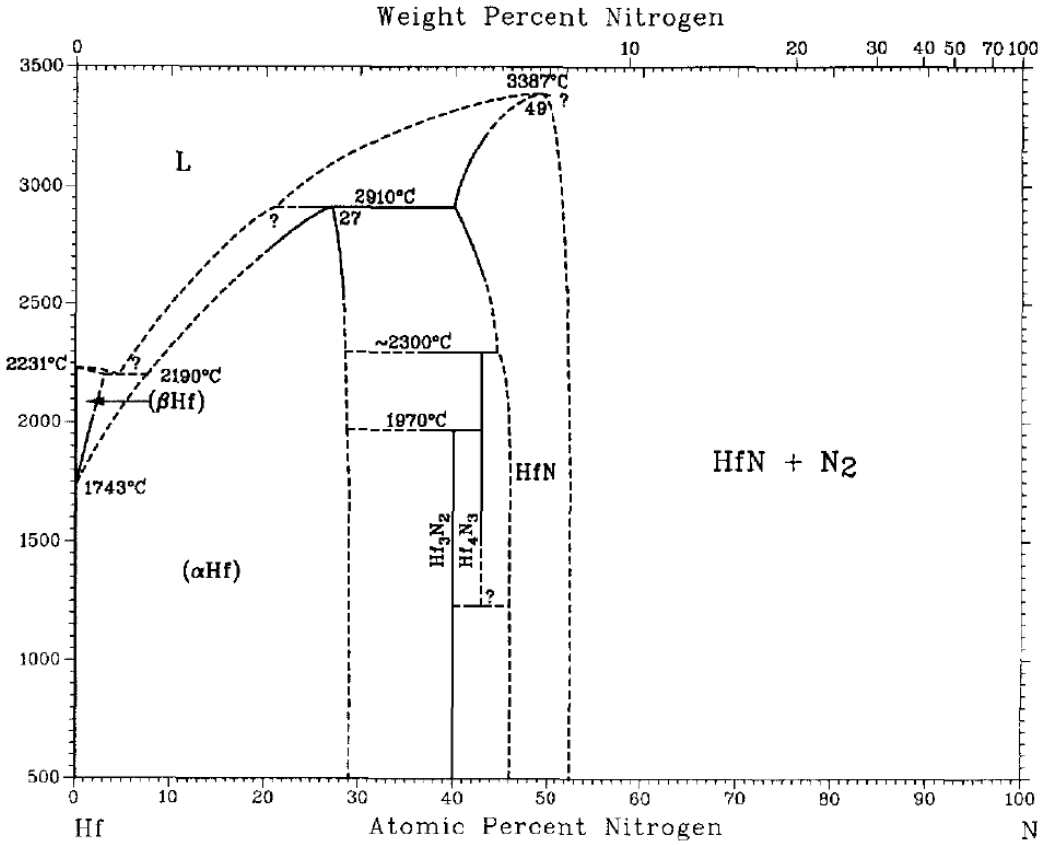

Figure 2.4: Phase diagram of Hf and N

Mechanical Properties

Like HfB_2 HfN shows a very high melting point of 3387 °C at a nitrogen content of 49 at% . Depending on its nitrogen content the melting point can slightly differ.[18] Though HfN has a high oxidation resistivity and good mechanical properties, HfB_2 beats it in all this issues. Therefore HfB_2 is much more studied than HfN.
The strength of HfN is lower than the strength of HfB_2 due to the more covalent nature of the chemical bonds.[20] Thin films of HfN obtained via PVD have a strength of 21 GPa and a Young's modulus of 224 GPa. [21]

2.2.3 Hafnium Films

Structure and Chemical Bonds

To determine the influence of the non-metals in hafnium based compounds on the oxidation behaviour, temperature resistivity and oxygen diffusion also pure hafnium thin films were analysed. Hafnium has a hexagonal close packed (hcp) crystal structure at room temperature. At 1770 °C it undergoes a phase transition from the α-Hf hcp to β-Hf with a body centred cubic (bcc) structure.[22]

Mechanical Properties

Hafnium has a melting point of 2233 °C, which is significantly lower than the melting points of HfB_2 and HfN. Also the strength (12 GPa) and the Young's modulus (94,5 GPa)[23] of sputtered hafnium thin films distinguishes a lot from the thin films of HfB_2 and HfN.

2.2.4 Oxidation

Like mentioned before, the oxidation behaviour of thin films is very important if a material is used in the aviation industry, due to the permanent exposure to an oxidising environment.

When HfB_2 or HfN is brought into contact with air at a high temperature (~700 °C) it oxidises and forms a passive oxidation protection layer containing B_2O_3 and HfO_2 in the case of HfB_2 (reaction 2.1) or only HfO_2 in the case of HfN (reaction 2.2).[24] In comparison pure hafnium already starts to oxidise at ~350 °C (reaction 2.3).[25]

$$HfB_2 + \frac{5}{2}O_2 \rightarrow HfO_2 + B_2O_3 \tag{2.1}$$

$$HfN + O_2 \rightarrow HfO_2 + \frac{1}{2}N_2 \tag{2.2}$$

$$Hf + O_2 \rightarrow HfO_2 \tag{2.3}$$

In case of HfB_2 the rate limiting step of the reaction is the transport of oxygen through B_2O_3. The mass gain, originating from the formation of HfO_2 is therefore diffusion limited. Between ~1100 °C and ~1400 °C B_2O_3 starts to evaporate, resulting in mass loss. The other phenomena, occurring when oxidising HfB_2, is that liquid boron accumulates just beneath the surface of the oxide, suppressing oxygen from diffusing into the material.[26] It is assumed that because of the presence of boron in the oxide layer HfB_2 forms thinner, more resistant oxide layers compared to HfN.

Looking at the oxidation of HfN the density of the oxide layer depends on the ratio of nitrogen in the compound. At a stochiometry of HfN_{75} a very dense oxide is build, which is desired in long time application of protective coating.[24]

3 Diffusion

Not only the oxidation behaviour of HfB_2, HfN and Hf thin films but also the oxygen diffusion behaviour through the obtained oxide layers and subsequently into HfB_2, HfN and Hf were analysed to determine if the non-metal elements in HfB_2 and HfN thin films have an influence on the oxygen diffusion compared to the oxygen diffusion of Hf and if the oxide layer of HfB_2 and HfN provides a better protective layer than Hf.

Diffusion is a process in which particles are transported due to random molecular motion, following Brownians law of motion which leads to the homogenization of a system with a given concentration gradient. Though a single atom motion can not be monitored, the flux of the particles can. Adolf Fick developed two laws for diffusion. In his first law (3.1) Fick describes the particle flux J in an unit area saying that J is proportional to the concentration gradient in that unit area, with c being the concentration of the diffusing particles, x the space coordinate and D the diffusion coefficient. Diffusion takes place in the direction of decreasing concentration, that is why a negative sign is in the equation.

$$J = -D\frac{\partial c}{\partial x} \tag{3.1}$$

Fick´s second law (3.2) shows the relationship between a temporal and a local concentration gradient and can therefore describe transient diffusion. The concentration after a certain time at a certain point can be calculated.[27]

$$\frac{\partial c}{\partial t} = D\frac{\partial^2 c}{\partial x^2} \tag{3.2}$$

In figure 3.1 the oxygen diffusion process through an oxide layer and into a bulk material is illustrated where c_0 represents the concentration of the constant source of the diffusing oxygen and c_{bulk} represents the initial base concentration in the material. While oxygen diffuses into the bulk material in x-direction the concentration of the source stays the same.

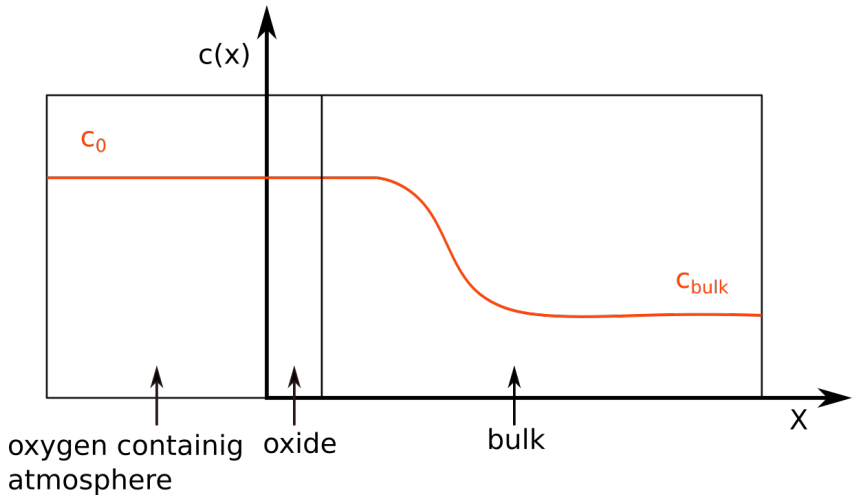

Figure 3.1: Schematic illustration of a diffusion profile in solids, with a constant source of oxygen

Measuring $c(x)$ the equations above could be solved by using the constant source solution [28] and further the diffusion coefficient of oxygen could be determined. Because of the limitation of the analytical instrument utilized in this thesis (ToF-SIMS) it is not possible to quantify the concentration of the diffusing oxygen without a highly expensive standardisation and thus not possible to determine the diffusion coefficient of oxygen in the analysed materials. Nevertheless a trend of the oxygen diffusion in the different materials at varying temperatures can be recognised.

4 ToF-SIMS

ToF-SIMS (Time of flight secondary ions mass spectroscopy) is an effective, sensitive and very universal method for chemical surface analysis. It has developed into a promising technique utilized in many industrial laboratories as well as research laboratories for surface characterization. Nearly every material is accessible with ToF-SIMS and detailed chemical information of both monolayer-depth profiles and monolayer-images with high mass and spatial resolution can be obtained.

Comparing ToF-SIMS with other surface analysing techniques it becomes clear why this method is so unique. For example Auger electron spectroscopy (AES) and X-ray photoelectron spectroscopy (XPS/ESCA), which are both broadly applied techniques in surface analysis, can not detect hydrogen or differentiate between isotopes. XPS on the other hand can yield information about functional groups, but not about big molecules. Other techniques such as infrared spectroscopy (IR), transmission microscopy (STM) or atomic force microscopy (AFM) are facing the same problematic with the detection of molecules.

Using a ToF-SIMS detailed information of elements and molecules can be obtained. A ToF-SIMS is able to detect all elements, differentiates between isotopes and even quantitative information can be obtained when using a standard. Apart from that no elaborate sample preparation is needed.[29]

4.1 Principle

The principle of ToF-SIMS is based on the emission of secondary particles as a result of bombarding the sample surface with highly energetic primary ions, typically Ar^+, Ga^+ or Cs^+. The particles emitted consist of electrons, atomic ions, cluster ions and neutral atoms or molecules, with the majority of the particles being of neutral character though only the emitted secondary ions are of interest. Collecting and analysing these, a mass spectrum of the sample surface, with very detailed chemical information in the region of up to ppb-level, can be generated, making ToF-SIMS a perfect method for trace analysis of surfaces.[30]

4.1.1 Formation of Secondary Ions

The sample surface is bombarded with ions from a finely focused primary ion beam, with a typical energy of 1-25 keV, which penetrates into the sample and transfers kinetic energy to the atoms of the sample, leading to a cascade of collisions. The penetration causes embedding of the primary ions into the sample surface as well as sputtering of surface particles. The sputtering process can be further subdivided into two processes:

- Change of sample surface
- Emission of surface particles

Possible changes of the sample surface are for example altering of the crystalline and molecular structure or fragmentation of molecules.
But the process which is most important to yield chemical information about the surface is the emission of surface particles, more precisely the emission of positively and negatively charged ions. These ions are called secondary ions and also include quasi-molecular ions like $(M+H)^+$, $(M-H)^-$ and $(M+Me)^+$(figure 4.1). Since

they emerge typically from the top layer, secondary ions yield direct chemical information about the sample surface. Neutral particles, electrons and photons only yield very little chemical information and can be neglected.

The fact that also thermally unstable ions, that cannot be vaporized, are emitted makes ToF-SIMS an outstanding and unique technique.[30]

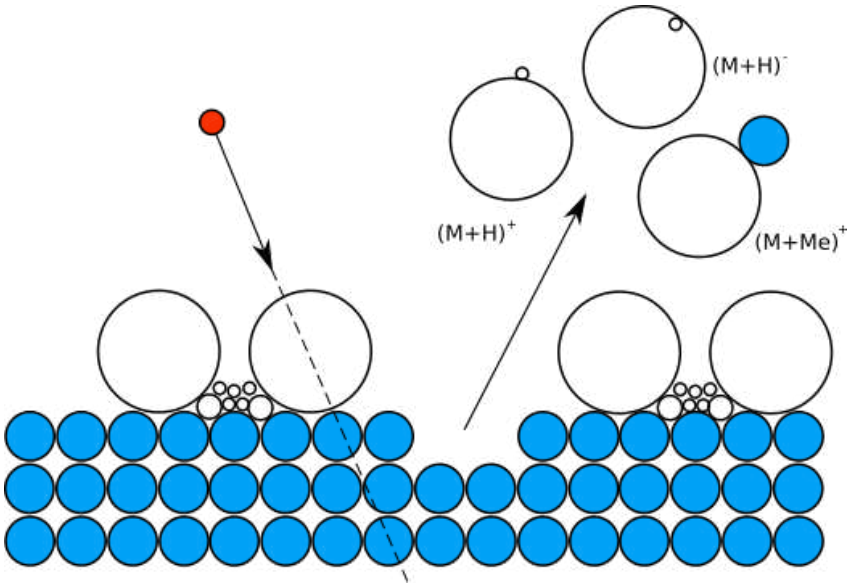

Figure 4.1: Formation of quasi-molecular ions through bombardment of a metal surface with primary ions. With the red dots symbolising the primary ions, the blue dots metal atoms, the big white dots molecules and the small white dots hydrogen atoms

4.1.2 Quantitative Description of Secondary Ions

In order to quantify the emission of secondary ions the relative coverage $\theta(M)$ of the surface particles M of the top layer is considered. $\theta(M)$ is the ratio of N (number of particles in the top monolayer of the sample surface) and N_0 (maximum possible number of particles in the top monolayer of the sample surface).

$$\theta(M) = \frac{N}{N_0} \tag{4.1}$$

Bombarding the sample surface leads to a decrease of the relative coverage with time, shown in equation 4.2. σ indicates the sputtering cross section, which is defined as the area of a monolayer corresponding to the average amount of particles M which are emitted due to bombarding the surface with a single primary ion. ν indicates the rate of primary ions arriving at the sample surface per second and cm^2.

$$M(\theta, t) = M(\theta, 0)^{-\nu\sigma t} \tag{4.2}$$

Equation 4.3 describes the probability that a certain type of secondary ion X_i^q is formed with a simultaneous disappearance of a particle M, due to bombardment of the sample surface with primary ions. This probability is called transformation probability $P(M \rightarrow X_i^q)$. The secondary ions $X_1^q, X_2^q, ..., X_i^q$ can occur in a neutral or charged form with q describing the charge of the newly formed particles. $P(M \rightarrow X_i^q)$ is defined as the ratio of the sputtering yield $Y_s(M)$ (average amount of particles M disappearing due to bombardment of a single primary ion) and the secondary particle yield $Y(X_i^q)$ (average amount of secondary ions of the type X_i^q

formed from particles M due to bombardment of a single primary ion).

$$P(M \rightarrow X_i^q) = \frac{Y(X_i^q)}{Y_s(M)} \tag{4.3}$$

Leading to equation 4.4, which describes the useful yield as the sum of the transportation probability $P(M \rightarrow X_i^q)$ and the total transmission of the spectrometer T_r.

$$Y_u = P(M \rightarrow X_i^q)T_r \tag{4.4}$$

If a metal surface is bombarded with 10 keV argon ions the sputtering yield $Y_s(M)$ is normally between 2 and 10 [31], whereby $Y_s(M)$ of molecules can be one power of ten higher.

Analysing metal surfaces, typically positive secondary ions are emitted (in addition to neutral compounds). A trend in the increasing secondary sputtering yield $Y(X_i^q)$ can be recognised correlating to a decreasing ionization energy of the metals. Generally $Y(X_i^q)$ of alkali metals can be up to 1 though most metals have a $Y(X_i^q)$ of 10^{-4} to 10^{-6}. The yield of cluster ions Me_n^+ decreases with increasing n.[29]

4.2 Main Components

ToF-SIMS distinguishes depending on the model. For this theses a TOF.SIMS5 (IONTOF GmbH, Münster, Germany) was used. Figure 4.2 shows an illustration of the characteristic components of a TOF.SIMS5. The yellow gun on the left side

is the Liquid metal ion gun (LMIG) which is utilized to generate secondary ions. Both red guns on the right side are sputter guns, which are utilized to remove the sample surface layer by layer. The blue unit in the middle shows the extractor, which draws in the generated secondary ions, and the ToF-Analyser, which analyses the secondary ions according to their mass-to-charge (m/z) ratio. The white unit between the sputter guns and the analysing unit is the flood gun, which compensates undesired surface charges.

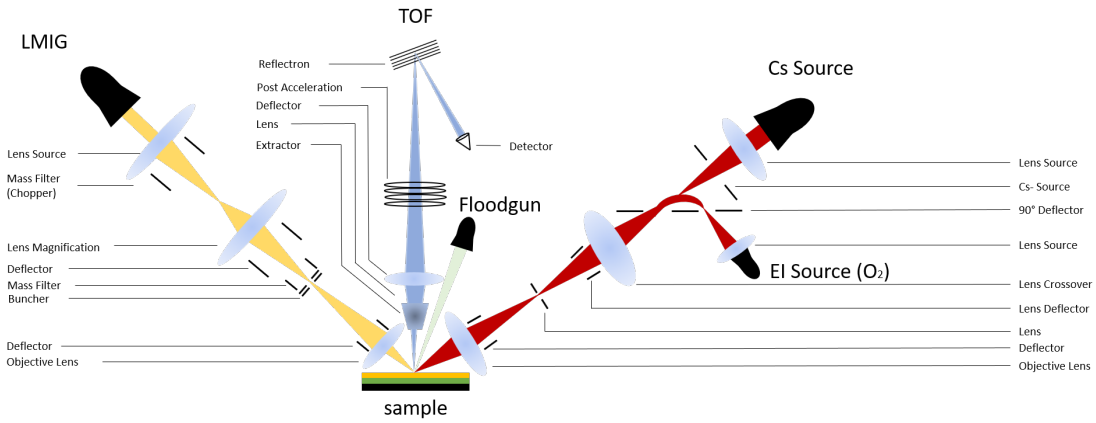

Figure 4.2: Illustraion of a TOF.SIMS5 from the IONTOF GmbH

4.2.1 Primary Ion Guns

A primary ion gun releases pulsed beams of primary ions, which then generate secondary ions emitted from the sample surface. Distinguishing between two different primary beams, an analysing beam (producing secondary ions that are analysed) and a sputtering beam (removes material from the sample surface) makes it possible to generate depth profiles and even 3D images. Figure 4.3 shows an illustration of an operating analysis and sputter beam.[32] In TOF.SIMS5 the Liquid metal ion gun LMIG provides the analysing beam and the dual source column DSC, contain-

ing two individual primary guns, provides the sputtering beams.

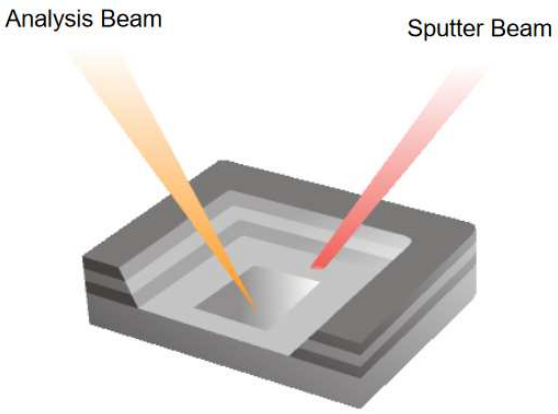

Figure 4.3: Illustration of both analysis and sputter beams[33]

Liquid Metal Ion Gun LMIG

Historically the primary ions used for ToF-SIMS have been Ga^+ and In^+, providing a good spatial resolution but lack a sufficient desorption efficiency.[34]
In the last years it became common to use gold [35] or bismuth cluster LMIGs to improve the ToF-SIMS imaging. Bismuth also stands out because of its relatively low melting point in contrast to gold, which has a relatively high melting point and additionally tends to vaporise at an evanescent pressure.
TOF.SIMS5 uses a bismuth emitter as primary analysing gun, but instead of a pure bismuth reservoir a MnBi alloy is utilized providing a more stable emission current. The MnBi-reservoir is linked to a wolfram needle that is connected to a heater filament which is further connected to two electrical feedthroughs, passing through an insulating holder. In front of the needle an extractor is placed. The heating filament holds the temperature just as high, so that the metal reservoir melts and coats the wolfram needle with liquid bismuth. Since the extractor is supplied with

a high negative voltage (-5 to -10 kV) and the electrical feedthroghs with a high positive voltage the metal ions are attracted to the extractor and the released electrons to the positive voltage, so that the positively and negatively charged particles are moving into different directions. The positively charged bismuth ions on the tip of the wolfram needle are in an equilibrium between surface tension and electrical forces, building a cone from which ions are emitted with a constant flux, depending on the extraction voltage. Figure 4.4 shows an illustration of a LMIG.[32]

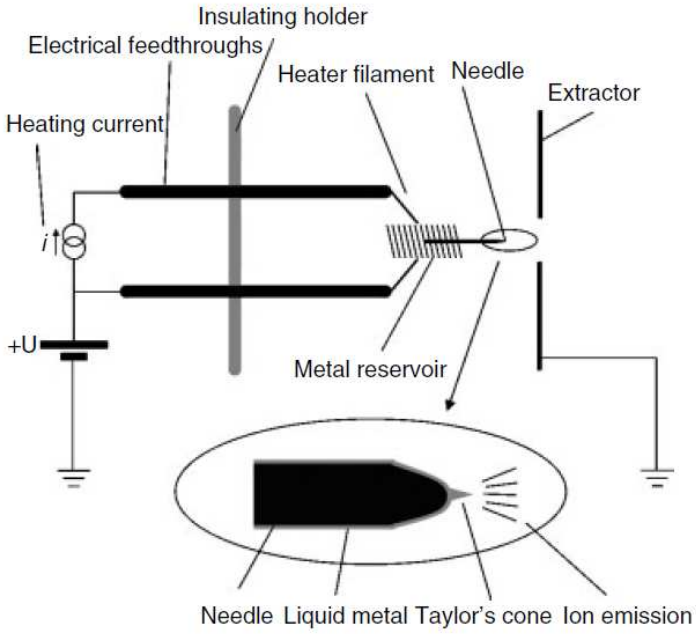

Figure 4.4: Illustration of a general LMIG utilized for ToF-SIMS[36]

Since a vary of different bismuth ion clusters are emitted from the BiMn emitter (Bi^+, Bi_2^+, Bi_3^+, Bi_4^+, Bi_5^+, Bi_6^+, Bi_7^+, Bi^{2+}, Bi_3^{2+}, Bi_5^{2+}, Bi_7^{2+} and Bi_5^{3+}) as well as manganese ions a mass filter, consisting of two chopper electrodes and an electrical field, selects between the different species. The first chopper pulses the beam into

packages, which are separated due to their m/z ratio in an electrical field. The desired species is selected with the second copper, which only lets one species pass through. Figure 4.5 shows a schematic of such a mass filter.

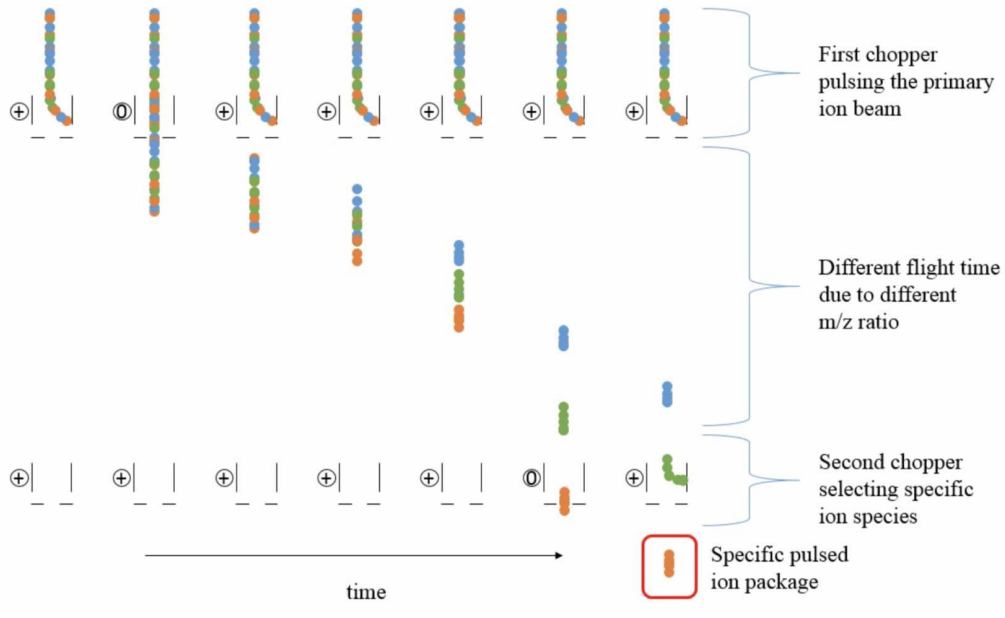

Figure 4.5: LMIG mass filter for selection of specific primary ion cluster species[37]

The secondary ions, emitted from the sample surface, are influence by the choice of the utilized bismuth ion cluster. Using Bi^+ as the primary ion the maximum yield of secondary ions can be obtained as well as the most fragmentation. Analysing lager organic molecules bigger bismuth cluster should be used in order to reduce the fragmentation.

For 2D surface analysis a ToF-SIMS setting with only a LMIG is totally sufficient, for depth profiles however it is necessary to additionally use a sputtering gun.[32]

Dual Source Column DSC

SIMS depth profiles are typically obtained with primary beams of Cs^+-, Ar^+- or O_2^+-ions. TOF.SIMS5 is equipped with a DSC of both a caesium emitter and an electron impact (EI) gas ion source. The caesium emitter consists of a surface ionisation source, emitting Cs^+ ions, which further generate mostly negative secondary ions. The EI source is commonly fed with oxygen but can also be fed with noble gases like argon. In a gas source sputter gun a circular filament cathode induces electrons that bombard the gas and generate primary ions, which are led into the right direction by an extraction field. Sputtering with O_2^+ generates mostly positive secondary ions.[32]

The secondary ion yield is influenced by the primary ions used (Cs^+ or O_2^+) and by the kinetic energy of the sputtering projectiles (0,25 keV - 2 keV).

4.2.2 Analyser Unit

The secondary ions are accelerated by an extractor into a field-free drift region and are subsequently analysed due to their m/z ratio in a time of flight mass spectrometer. The extractor consists of an electrostatic field and can operate in a positive or a negative mode. If the electrostatic field is positively charged only negative charged secondary ions are collected, this setting is called negative mode. The positive mode works the other way around.

Accelerating the secondary ions to the same nominal kinetic energy E_{kin}, which is the sum of the potential U_a and the elementary charge e, they will access the field-free drift region with velocities ν according to their mass m:

$$E_{kin} = \frac{m\nu^2}{2} = eU_a \tag{4.5}$$

With L_d indicating the length of the field-free drift section, the time T needed for

a secondary ion to reach the detector is:

$$T = \frac{L_d}{\nu} = L_d(\frac{m}{2eU_a})^{\frac{1}{2}} \tag{4.6}$$

ToF-SIMS can detect either all negative or positive ions at once, a feature that a sector field MS and a quadrupole MS lacks. In addition, ToF-SIMS is a very sensitive method, especially if it is enhanced with a reflectron. A reflectron is used to neutralize energy spread of the secondary ions due to the fact that not all ions are accelerated at the exact same position and therefore have a different kinetic energy when entering the field-free drift section. As a consequence, ions with identical mass do not have the same velocity and therefore do not reach the detector at the same time. The mass resolution suffers from that. A reflectron consists of two field-free drift sections and an ion mirror (figure 4.6). The secondary ions enter the first drift section with different kinetic energies leading to the ion mirror, an electrostatic field, where they are slowed down, stopped and finally accelerated in the opposite direction. Ions with a higher kinetic energy penetrate the electrostatic field further than ions with a lower kinetic energy, so that both ions leave the electrostatic field and enter the second field-free drift section with the same velocity and reaching the detector at the same time,[38] resulting in a mass resolution of up to 35000.[39]

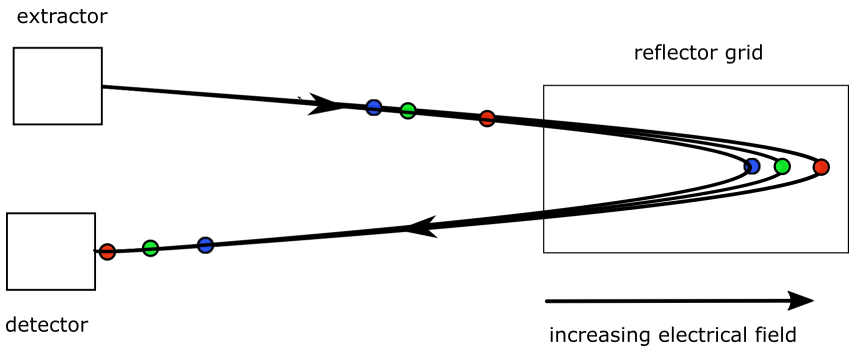

Figure 4.6: Illustration of a reflectron utilized to improve the mass resolution

4.2.3 Flood Gun

Analysing an insulating material, charging of the sample can be a problem because of altering intensity of the peaks in connection with surface charges, causing lower and broader peaks with rising charges or even loosing all intensity of the peaks.[40] To overcome this problem TOF.SIMS5 is equipped with an electron flood gun.
When an insulating sample surface is bombarded with primary ions the ions are implanted into the surface which leads to an electric potential on the surface. Due to the potential no secondary ion emission of negative ions can take place. Moreover the kinetic energy of the positive secondary ions will rise. The flood gun releases electrons between the primary ion pulses to neutralize the positive charge.[41]

4.3 Measuring Modes

TOF.SIMS5 operates in different measuring modes, offering either a high mass resolution or a high spatial resolution.
If a maximal mass resolution is required the primary ion beam should be very shortly pulsed, but if the beam pulse is to short it extends the measuring time rapidly in addition to a great loss of spatial resolution. Introducing a buncher between the primary ion source and the sample surface a longer pulse can be shortened by compressing it with an electrical field. The ions in the end of the pulse are accelerated by a potential gradient so they can catch up with the ions in the front. Typically a 20 ns pulse can be shorten into a 1 ns pulse.
Requiring a high spatial resolution, the primary ion beam has to be of high brightness and provide a low energy spread in order to assure that only ions from a certain point of the source, with a limited angular acceptance, reach the sample and minimise chromatic abberration. In order to achieve these requirements three lenses shape the beam to optimise the spatial resolution.[32]

Four different measuring modes are described beneath. Figure 4.7 shows their different lens settings.

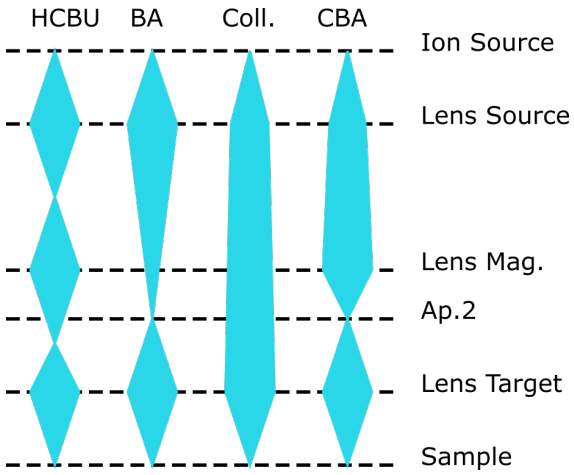

Figure 4.7: Illustration of analysis primary ion beams used for different measurement settings

4.3.1 High Current Bunch Mode HCBU

The HCBU mode is used when a high mass resolution or a low limit of detection is required. The analysis primary ion beam is bunched and has a very high intensity (15 nA - 17 nA) thus a mass resolution of $> 11\,000$ can be obtained. However, the bunched primary ions cannot be focused very well and therefore a large diameter of the beam is obtained, leading to a low spatial resolution.

4.3.2 Burst Alignment BA

To obtain images with a high spatial resolution the BA mode is used. In this mode the analysis primary ion beam is finely focused thus a high spatial resolution of

up to 250 nm can be obtained. To reach a high enough beam current, the pulse duration has to be long, which leads to a very low mass resolution of ~200.

4.3.3 Collimated Mode

Another mode for imaging is the collimated mode obtaining a spatial resolution of up to 100 nm but with a very low current and low mass resolution.[42]

4.3.4 Collimated Burst Alignment CBA

A very novel mode, which has been developed in 2013 at Tu Vienna[43] is the CBA mode, a mixture of BA and Collimated Mode providing images with high spatial resolution (<100 nm) and a mass resolution of >6000.

A summary of the basic data for all measuring modes discussed above is shown in table 4.1.

	HCBU	BA	CBA	Collimated Mode
DC current (nA)	14-16	0.4-0.75	0.07	0.05
Mass Resolution	11000*	200*	6000	200*
Spatial Resolution (nm)	2000-10000*	250-300*	96-136	100*

Table 4.1: ToF-SIMS measuring modes and there basic data[43]. All values marked with a * are from the IONTOF helpfile

5 Sample Preparation

Hf, HfB_2 and HfN were deposited via PVD onto a substrate. Several substrates were utilized but it turned out that α-Al_2O_3 (Sapphire) worked best for both the PVD process and the subsequent ToF-SIMS measurements. After the coating the samples where tempered at different temperatures to oxidise the obtained hafnium based thin films. Additionally a small selection of the samples were tempered again in an ^{18}O atmosphere.

5.1 Physical Vapour Deposition PVD

PVD is a technique used to produce thin films due to a physical process, where a condensed phase goes to a vapour phase which in turns condenses on a substrate. One of the most common PVD processes is sputtering. In this process a target (source material) is bombarded by positive ions (often argon) from a plasma, resulting in a vapour. The vapour is then transported through a vacuum to the substrate where it condenses and builds a uniform film.

Magnetron sputtering is the most utilized application for film growth by sputter deposition with the advantages of low temperature, speed and little damages of the films. In this process additionally to an electrical field also a magnetic field is generated behind the target. Due to the overlapping of both fields the ions in the plasma move in a spiral over the target, causing more ionizing collision with neu-

tral particles, which leads to a higher number of ejected particles from the target surface. (Figure 5.1)

Depending on the material of the target, either direct current (DC) magnetron sputtering or radio frequency (RF) magnetron sputtering is used. Using DC magnetron sputtering the target has to be electrically conductive in contrast to RF magnetron sputtering, which does not require an electrical conductive target.[44]

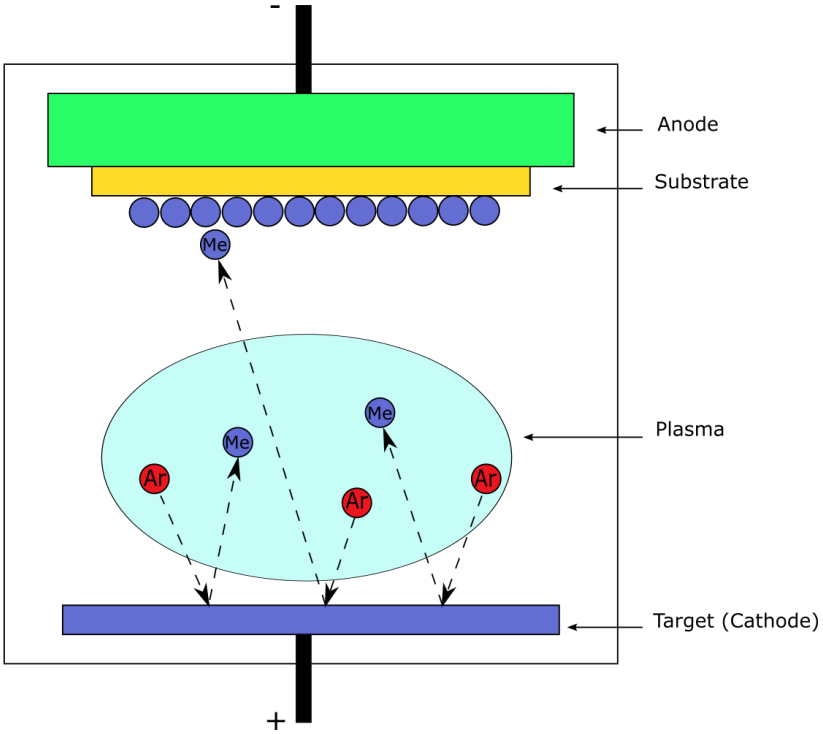

Figure 5.1: Illustration of a magnetron sputtering process

For this thesis thin films of Hf, HfB_2 and HfN were obtained with an in-house developed magnetron sputter system. Hf and HfB_2 targets of Plansee Composite Materials GmbH were used. Hf and HfB_2 thin films were obtained in pure argon atmosphere (purity 99,999%) in contrast to the HfN thin films, which were obtained in a gas mixture of argon and nitrogen. Before starting the deposition process, targets and substrates were sputter-cleaned in pure argon atmosphere at a pressure

of 5,0 Pa. The targets were operated in DC mode with a working gas pressure of 0,58 Pa. For HfN and HfB_2 the substrate temperature was set to 550 °C whereas for Hf the temperature was set to 350 °C, with a bias voltage of 65 V for all materials. The process was carried out for one hour and thin films of ~2 μm thickness were obtained.

5.2 Oxidation

For the oxidation a differential thermal analysis (DTA)/-thermo-gravimetric analysis (TGA) system, equipped with a Rhodium furnace (Netzsch STA 449 F1) was used. DTA/TGA provides both thermal information and information about mass loss or gain during a temperature cycle.
The samples were placed into a Al_2O_3 crucible and heated up at a heating rate of 10 K/min in an atmosphere of synthetic air. A mass to temperature diagram was obtained and, because of the mass gain at a certain temperature, the onset of the oxidation could be determined. Figure 5.2 shows a mass to temperature diagram of Hf, HfB_2 and HfN.

It is clearly visible that the mass gain of HfB_2 is a lot higher compared to that of Hf and HfN. Like mentioned in section 2.2.4, when oxidising HfB_2 B_2O_3 is formed in addition to HfO_2. This leads to a higher mass gain in the beginning of the oxidation but also to a mass loss starting at ~1200 °C due to the evaporation of B_2O_3. In contrast Hf and HfN both show a mass gain until ~850 °C for Hf and ~1100 °C for HfN, which is followed by a constant mass signal. Hf shows a small peak at the transition from mass growth to a constant mass signal, probably because a small part of the oxide layer had flaked off. The determined oxidation onset temperatures of Hf, HfN, HfB_2 are summarized in table 5.1.

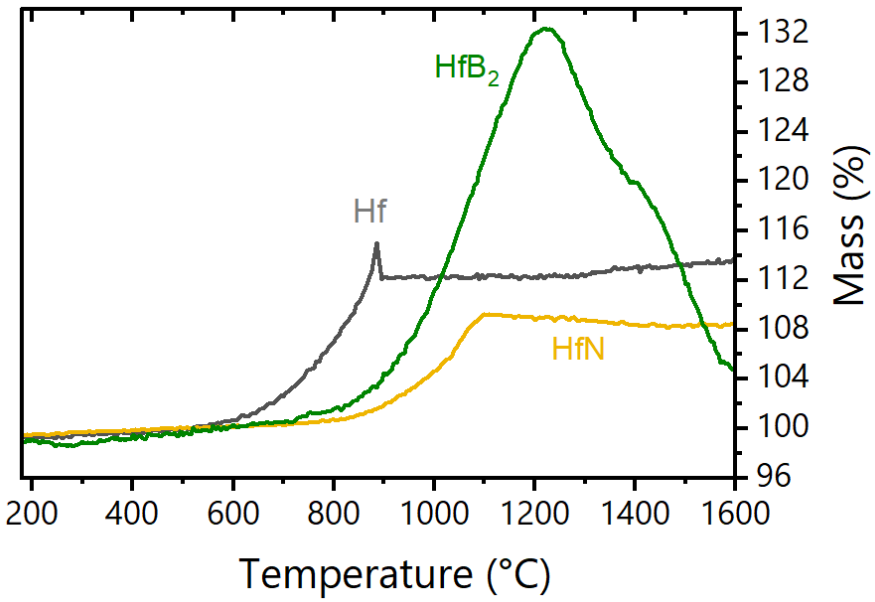

Figure 5.2: Temperature to Mass Diagram of Hf, HfN, HfB_2 obtained in a dynamic DTA/TGA Measurement

	Hf	HfN	HfB_2
Temperature of onset (°C)	640	840	800

Table 5.1: Oxidation onset temperatures of Hf, HfN, HfB_2

After the onset temperatures were determined, every material was oxidised isothermal at the respective oxidation onset temperature as well as 100 °C above and beneath. Due to technical issues Hf could only be oxidised at the onset temperature and 100 °C beneath.

For the isothermal measurement, the samples were heated up at a heating rate of 20 K/min in a pure helium atmosphere. When the desired temperature was reached, synthetic air (50 ml/min) was let into the crucible. After a certain time the valve was closed and the sample was cooled down at a rate of 25 K/min in a

	Hf	HfN	HfB_2
Temperature (°C)	540	740	700
Duration (min)	120	120	120
Temperature (°C)	640	840	800
Duration (min)	60	60	60
Temperature (°C)		940	900
Duration (min)		30	30

Table 5.2: Temperatures and durations of the oxidation of all materials analysed

pure helium atmosphere. Before the oxidation process the samples were thermally cleaned for 20 min at 110 °C. The different temperatures and oxidation durations are summarised in table 5.2.

As an example for the isothermal oxidation a time to mass diagram of HfN is showed in figure 5.3. The isothermal oxidation of the other materials show a very similar course.

It is clearly visible that the higher the temperature, used for the oxidation, the steeper is the curve of the mass gain, indicating that the oxide layer is formed quicker the higher the temperature is. Due to this fact, the different oxidation durations (table 5.2) were chosen to prevent the oxide layers in the higher tempered samples from becoming too thick or from complete oxidation of the material.

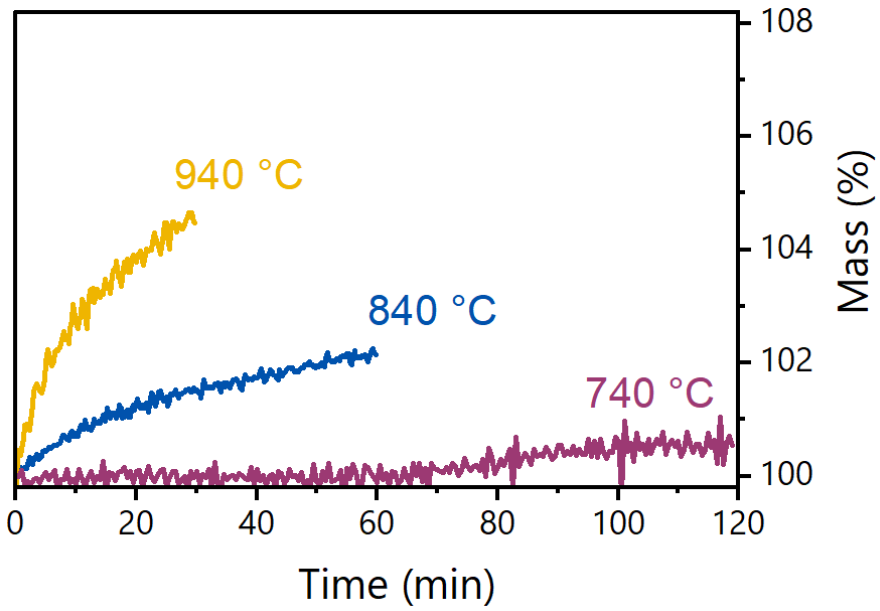

Figure 5.3: Temperature to mass diagram of HfN obtained from isothermal oxidation with a DTA/TGA

5.3 Treatment with ^{18}O

A sample of each material (Hf, HfB_2 and HfN), which had previously been oxidised, was tempered, in an ^{18}O atmosphere, in an in-house developed tube furnace. The samples were placed onto the quartz tube and the oven is evacuated and purged with nitrogen three times. Afterwards it is evacuated once more and finally 200 mbar of ^{18}O were let into the oven. The oven is then heated up, at a heat rate of 10 K/min, until the desired temperature is reached, held at that temperature for 30 min and then cooled down.

The samples were heated up to the same temperature at which they had been oxidised before. The samples used for the treatment with ^{18}O are summarised in table 5.3.

	Hf	HfN	HfB_2
Temperature (°C)	640	840	840
Duration (min)	30	30	30

Table 5.3: Temperatures and durations of the treatment with ^{18}O of all materials analysed

6 Analysis

6.1 TOF-SIMS

6.1.1 Measuring Settings

All samples were measured in the above described HCBU mode, to obtain depth profiles with high mass resolution.

When measuring in the HCBU mode it can be decided between an interlaced and non-interlaced measuring setting. The difference between these two settings is the arrangement of the analysis and the sputter beam. For a mass interval of 1-371 and an analysing beam of 20 ns a measuring cycle takes 65 μs. Which means that most of the time in a cycle is used by the sputter beam.

When measuring in the interlaced setting the LMIG pulse is directly followed by sputtering and electron flooding in contrast to the non-interlaced setting, where a certain number of LMIG pulses is followed by a pause. After the pause a certain period of sputtering and electron flooding takes place. The duration of both analysis beam and sputter beam can individually be adjusted. (Figure 6.1)

If possible, the interlaced mode is used, because it is a lot faster than the non-interlaced mode and in addition the maximum secondary ion yield can be obtained. For non-conducting samples though it is sometimes not avoidable to use the non-interlaced mode, to compensate surface charging. In this thesis all samples were measured in the interlaced measuring mode.

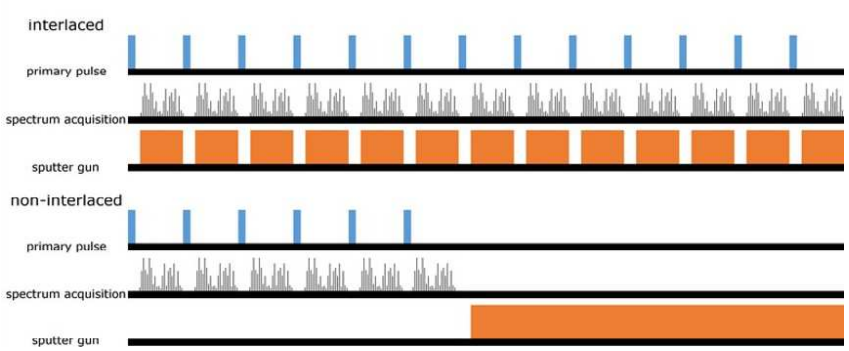

Figure 6.1: Illustration of the interlaced and non-interlaced setting[45]

Rastering of the surface was set to sawtooth. In that mode the beams start at the upper left corner and work their way down, by a serpentine line, to the lower right corner. 128 x 128 pixels were captured. The field of view was set to 100 μm x 100 μm by the navigator and the crater size was set to 300 μm x 300 μm in the DSC settings.

No stop conditions were set, because each depth profile had to be stooped individually after reaching the substrate. All setting are listed in figure 6.2.

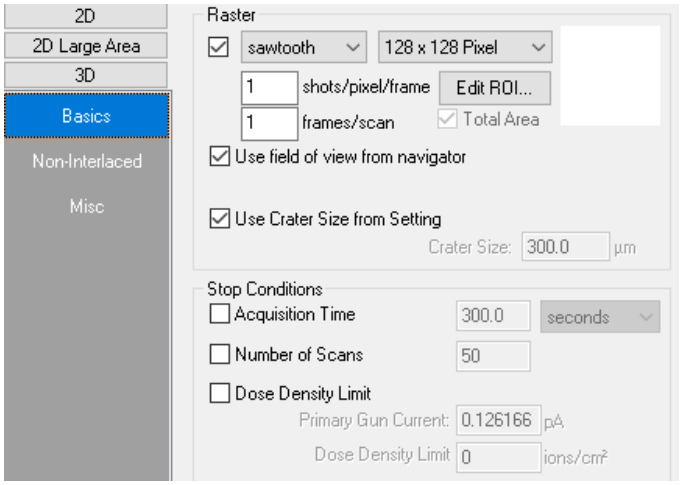

Figure 6.2: Measuring settings used for all samples

In figure 6.3 the crater obtained from one of the measurement is shown. The red square encloses the analysing field.

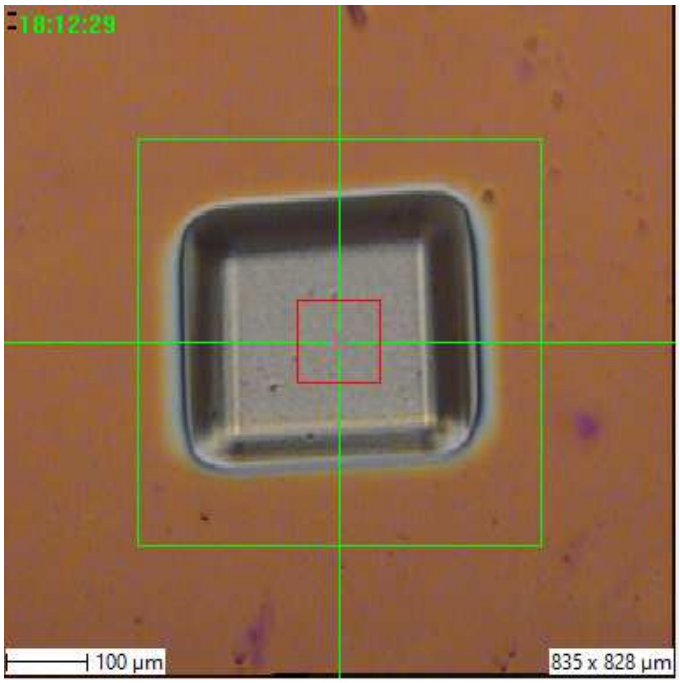

Figure 6.3: Crater of the Hf thin film oxidised at 540 °C

6.2 Scanning Electron Microscope SEM

To determine the oxide scale and thin film thickness images of cross sections of the films were obtained by using a Scanning Electron Microscope (SEM, FEI Quanta 250 FEGSEM operated at 15 kV). The images were compared to the depth profiles obtained by ToF-SIMS measurements.

6.2.1 Principle

With a SEM images of a sample surface can be obtained by scanning the surface with a finely focused beam of primary electrons. The primary electrons are emitted from a cathode, then accelerated, due to a voltage difference between the cathode and an anode, and finally focused with a lens system. When the primary electron beam reaches the sample surface secondary electrons and backscattered electrons are formed and a range of electron-specimen interaction takes place leading to an image with a very high spatial resolution.

The SEM used for this thesis is equipped with a field-emission gun FEG. Using a FEG electrons are emitted from a single crystal tungsten tip due to a very high potential difference between the tungsten tip (cathode) and the anode leading to the emission of electrons from the Fermi level through a tunnelling process. FEG requires a very high vacuum under 10^{-6} Pa to prevent the tip radius from being destroyed by ion bombardment. A FEG guarantees a brighter and more coherent primary electron beam resulting in a better image quality with a spatial resolution beneath 1 nm.[46][47]

7 Results and Discussion

7.1 ToF-SIMS Measurements

To determine the influence of non-metals on the oxidation and oxygen diffusion behaviour of hafnium based thin films depth profiles of the as-deposited thin films, the oxidised thin films as well a the with ^{18}O treated thin films were obtained with a TOF.SIMS5 and analysed.

The depth profiles are presented in an intensity to sputter time diagram. The sputter time represents the time during which the sputter gun was active.

All samples were measured in the negative mode because of two reasons. Firstly, to obtain an intensive oxygen signal (oxygen is much more sensitive in the negative than in the positive mode) and secondly, because in the positive mode the sputter gun is normally fed with oxygen which could have distorted the oxygen signal.

Like mentioned in chapter 4 ToF-SIMS is generally not a quantitative measuring method. Depending on the material the yield of the secondary ions can vary, therefore the intensity of the secondary ions does not correspond to the exact concentration. Nevertheless the depth profiles obtained are a unique method to show the course of significant elements in the thin films.

7.1.1 Hafnium Hf

First of all, depth profiles of the as-deposited (not oxidised) and the oxidised Hf samples were generated and the course of hafnium and oxygen through out the thin film was analysed. The courses of the analysed secondary ions are shown in figure 7.1, 7.2 and 7.3.

Two isotopes of oxygen ($^{16}O^-$ and $^{18}O^-$) were analysed to track the oxidation and the oxygen diffusion. ^{16}O is the most abundant isotope of oxygen (99,76 %[48]), and because of its high sensitivity in ToF-SIMS measurements and its high presence in the materials, especially in the oxide layer, the intensity of $^{16}O^-$ is partly above the saturation. Therefore the course of oxygen cannot be tracked correctly with $^{16}O^-$. Since ^{18}O is a lot less common $^{18}O^-$ never reaches the saturation and can be used to track the correct oxygen course.

The intensity of Hf^- is very low, due to the fact that metals naturally tend to form positive ions.

Like expected, the oxide layer of the sample oxidised at 640 °C is thicker than the sample oxidised at 540 °C even though the oxidation duration was shorter in the higher tempered sample. The interface between the oxide and the intact Hf layer is visible due to the drop of the oxygen signal.

Looking at the oxygen signal throughout the intact Hf layer, in the at 540 °C oxidised sample, a gradual decline followed by an increase can be recognised, indicating that oxygen diffusion takes place both from the oxidized side and from the substrate. The oxygen diffusion increased even more in the higher tempered sample, resulting in a much higher oxygen intensity throughout the whole film in comparison with the initial base concentration in the as-deposited film. In contrast to the lower tempered sample, in the higher tempered sample oxygen penetrates much further into the film, so that the oxygen signal overlays the signal from the diffusion of the substrate.

The Hf^- signal is constant both in the as-deposited as well as in the oxidised samples, which does not indicate that the actual concentration is the same in the oxide layer and in the Hf film. But it is save to say that the concentration of Hf is constant in each layer and that the oxide layer definitely contains Hf.

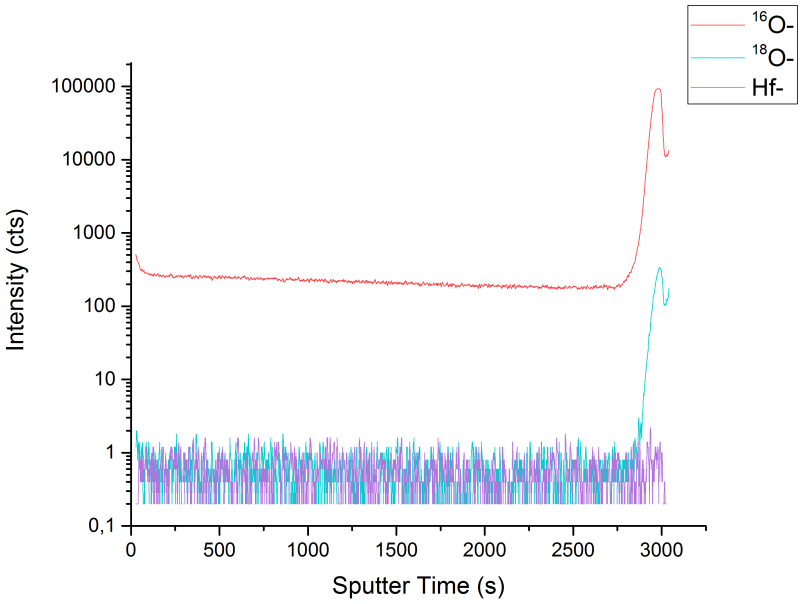

Figure 7.1: Hf as-deposited

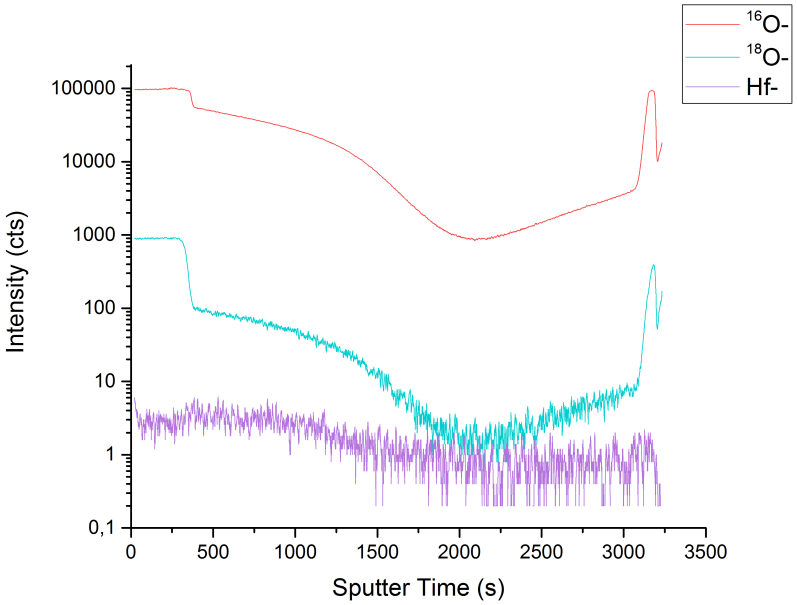

Figure 7.2: Hf oxidised at 540 °C for 2 h

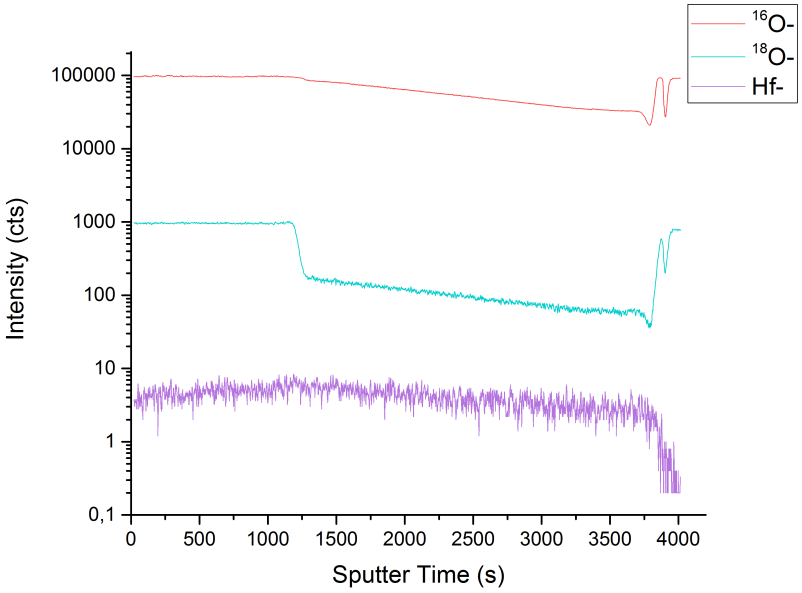

Figure 7.3: Hf oxidised at 640 °C for 1 h

7.1.2 Hafniumdiboride HfB_2

To analyse HfB_2 the same secondary ions tracked in the Hf measurements were used, with the addition of B^-. The courses of the analysed secondary ions are shown in figure 7.4, 7.5, 7.6 and 7.7.

Similar to the oxidation behaviour of Hf, the oxide layer on top of the HfB_2 film gets thicker the higher the temperature is. The oxide layer of the highest tempered samples is about four times thicker than the lowest tempered sample. In contrast to Hf though, two oxide layers are formed when oxidising HfB_2, probably due to the fact that hafnium oxide as well as boron oxide occur during the reaction.

Interestingly the intensity of B^- is higher in the outer than in the inner oxide layer contrary to the intensity of Hf^- which is higher in the inner layer compared to the outer layer. Knowing that every material yields a different amount of secondary ions this assumption must be regarded with caution. However it seems to be particularly true for Hf, since almost no signal is visible in the outer layer, but a clear signal can be seen in the inner layer.

Save to say though is that the oxygen diffusion into the HfB_2 layer both from the oxidized side and from the substrate is a lot lower compared to the oxygen diffusion in the Hf thin films. Only in the highest tempered sample a slightly higher oxygen diffusion originating from the the oxidised side, is visible, compared to the lower tempered samples, but the major part of the HfB_2 layer shows the initial base intensity measured in the as-deposited sample.

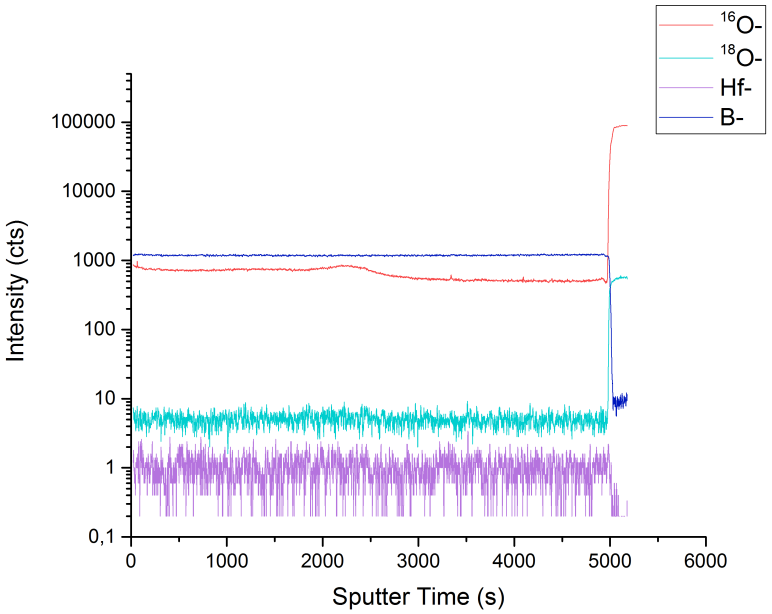

Figure 7.4: HfB_2 as-deposited

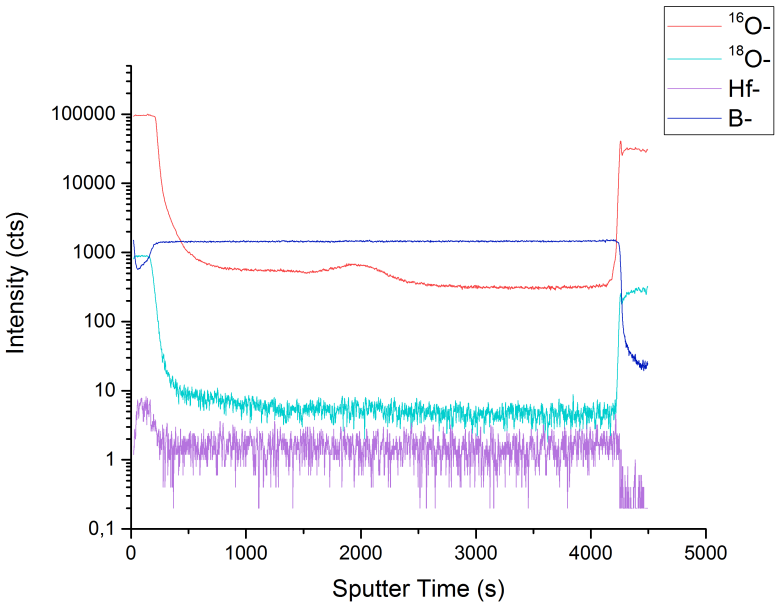

Figure 7.5: HfB_2 oxidised at 7000 °C for 2 h

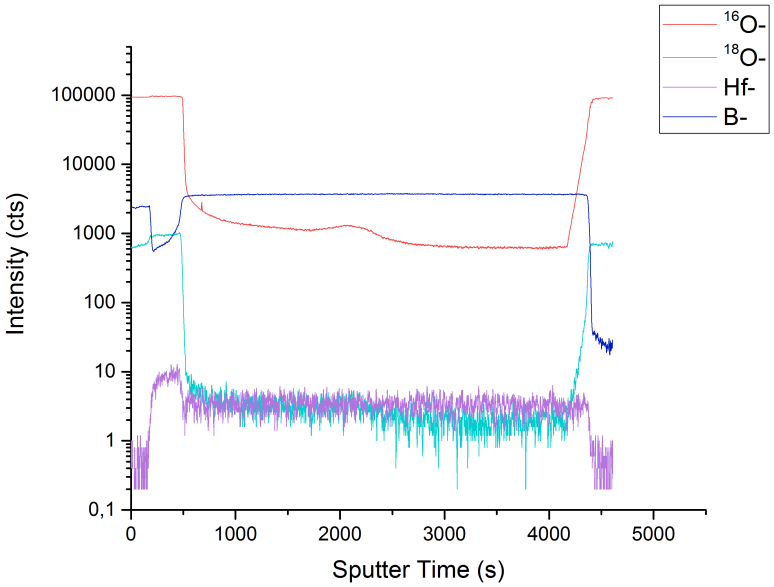

Figure 7.6: HfB_2 oxidised at 8000 °C for 1 h

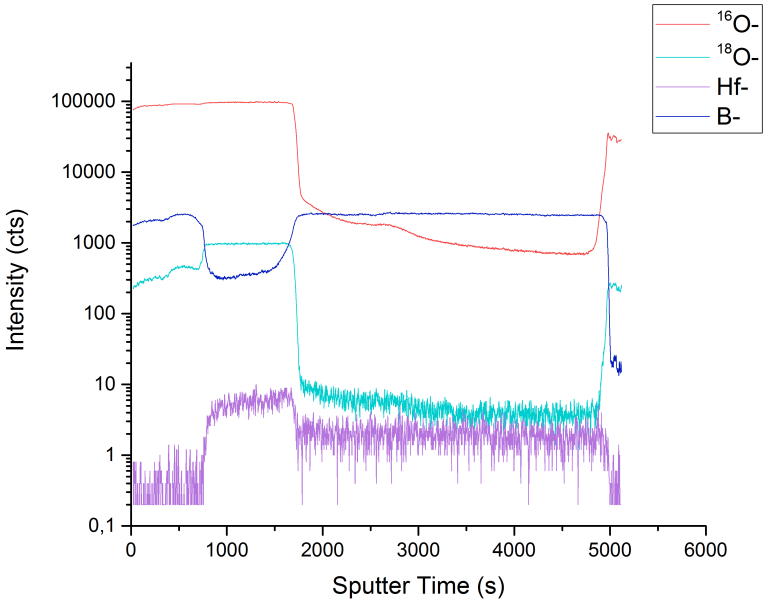

Figure 7.7: HfB_2 oxidised at 900 °C for 30 min

7.1.3 Hafniumnitrid HfN

For the analysis of HfN besides $^{18}O^-$, $^{16}O^-$ and Hf^- also HfN^- was tracked. HfN^- was used to indirectly track nitrogen since tracking nitrogen directly in the negative mode is very difficult due to the very low yield of N^-. The ToF-SIMS measurements of HfN are shown in figure 7.8, 7.9, 7.10 and 7.11.

The increase of the oxide thickness in correlation with temperature follows the same scheme as HfB_2. The oxide layer of the highest tempered sample has about quadrupled in the highest tempered sample but it seems that the oxide layers in total are thicker than the oxide layers of HfB_2.

Like HfB_2 HfN forms two different oxide layers when exposed to high temperatures indicated by a non-homogeneous $^{18}O^-$ course in the oxide layer. The $^{18}O^-$ signal in the outer oxide layer shows a strong fluctuation in contrast to the inner oxide layer, which shows a steady $^{18}O^-$ course.

Looking at the samples oxidised at 740 °C mainly a constant $^{18}O^-$ signal is visible in the oxide layer. Only in the very beginning of the measurement a slight fluctuation is visible, which indicates that the outer oxide layer is probably very thin. However, the sample oxidised at 840 °C shows a clearly visible difference in the $^{18}O^-$ signal. It seems that the outer oxide layer is still a lot thinner compared to the inner layer, but looking at the at 940 °C oxidised sample it seems that the outer layer has been rapidly growing and has become a lot thicker than the inner layer. The unsteady signal from the outer oxide layer, especially visible in the highest tempered sample, occurs probably due to surface charging, which is very likely when analysing insulating layers like oxides.

Looking at the oxygen diffusion in the HfN layer, the lower tempered samples show almost no diffusion and the major part of the HfN layer has the initial base intensity measured in the as-deposited sample. In contrast to HfB_2 though a slight oxygen diffusion from the substrate into the material is recognisable. However, the

oxygen diffusion in the highest tempered sample increased a lot compared to the lower tempered samples.

Comparing the oxygen diffusion in HfN and in HfB_2 thin films it seems that the lower tempered samples of both materials behave the same but in the higher tempered sample HfN is more permeable for oxygen than HfB_2.

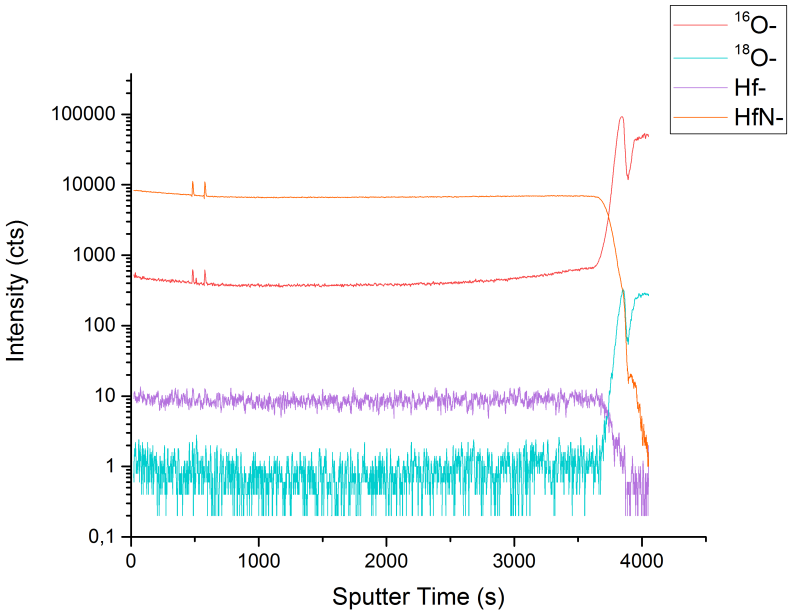

Figure 7.8: HfN as-deposited

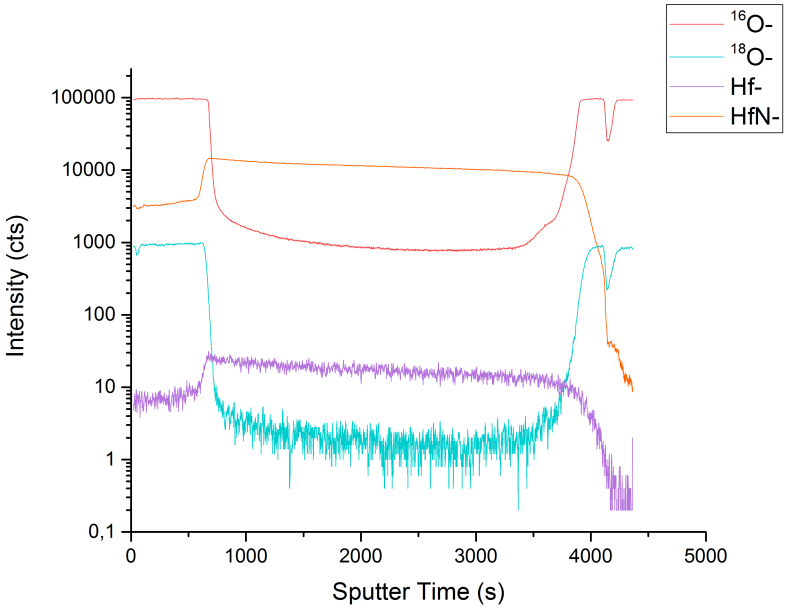

Figure 7.9: HfN oxidised at 740 °C for 2 h

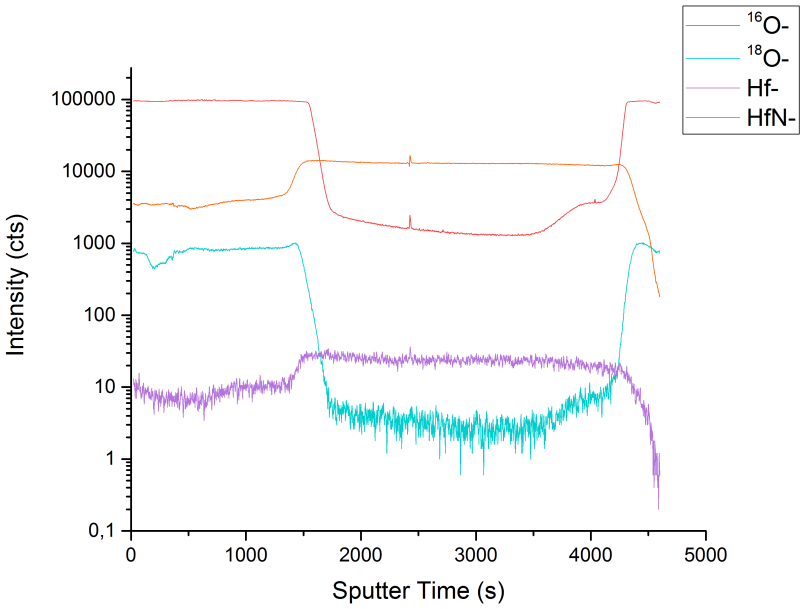

Figure 7.10: HfN oxidised at 840 °C for 1 h

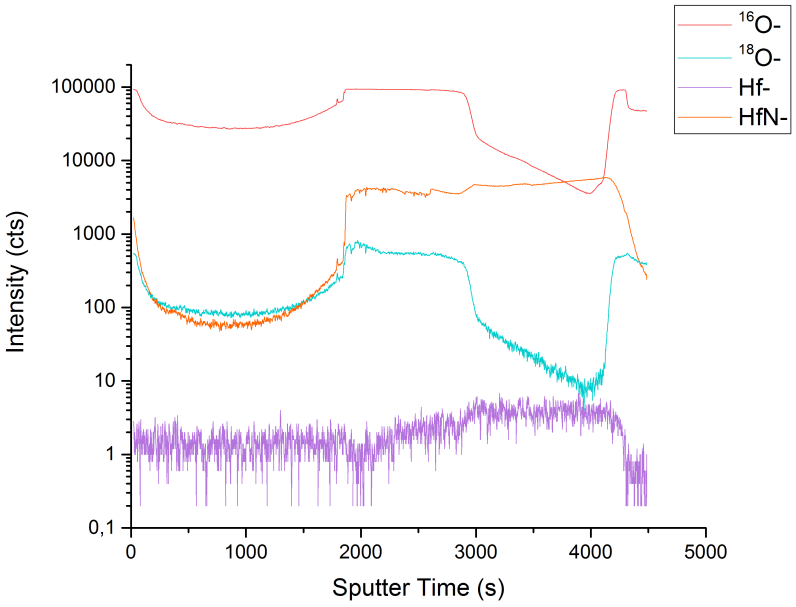

Figure 7.11: HfN oxidised at 940 °C for 30 min

7.1.4 Treatment with ^{18}O

To determine if oxygen can permeate through the respective oxide layer of Hf, HfB_2 and HfN and into the intact material beneath a depth profile before and after the treatment with ^{18}O was analysed and compared.

Heating the Hf thin film, which has previously been oxidised at 640 °C in synthetic air, again to 640 °C for 30 min in an ^{18}O atmosphere led to the complete oxidation of the thin film, unfortunately making it impossible to analyse the diffusion of ^{18}O in the Hf thin film.

The depth profiles with the courses of $^{18}O^-$ and $^{16}O^-$, before and after the oxidation with ^{18}O, of both HfB_2 and HfN are shown in figure 7.12, 7.13, 7.14 and 7.15.

Looking at HfB_2, like expected, the oxide layer grew as well when the sample was reheated but a part of the HfB_2 thin film was preserved. Comparing the $^{18}O^-$ signal after the treatment with ^{18}O with the depth profile from before, an increase

of the intensity is clearly visible, which indicates that oxygen can diffuse through the oxide layer. It is noticeable that the $^{18}O^-$ signal decrease after the interface of the oxide layer and the HfB_2 layer but that the signal is still relatively high in the end of the HfB_2 layer and does not drop to the initial base intensity of the as-deposited sample. Since only a smaller part of the thin film has not been oxidised and the drop of the $^{18}O^-$ signal is quite steep, especially when keeping in mind that the intensity axis is logarithmically scaled, it is possible that the initial base intensity of $^{18}O^-$ would be reached if more of the HfB_2 thin film was preserved. On the other hand it cannot be ruled out that the high intensity occurs due to a displace of ^{18}O from the oxide into the intact HfB_2 layer due to the sputtering process. However, it can definitely be said that the oxide layer does not completely protect the material from oxygen diffusion but it is questionable if the diffusion is really as high as indicated by the measurement.

The same effects can be recognised in the HfN thin film, but the oxide layer seems to be a lot thicker compared to that of HfB_2, making it even harder to say if the $^{18}O^-$ signal would have dropped further if more of the HfN material had been preserved. It would make sense to repeat the experiment but with a reduced duration of heating at the desired temperature and with an increase of the heating rate, to prevent further oxidation.

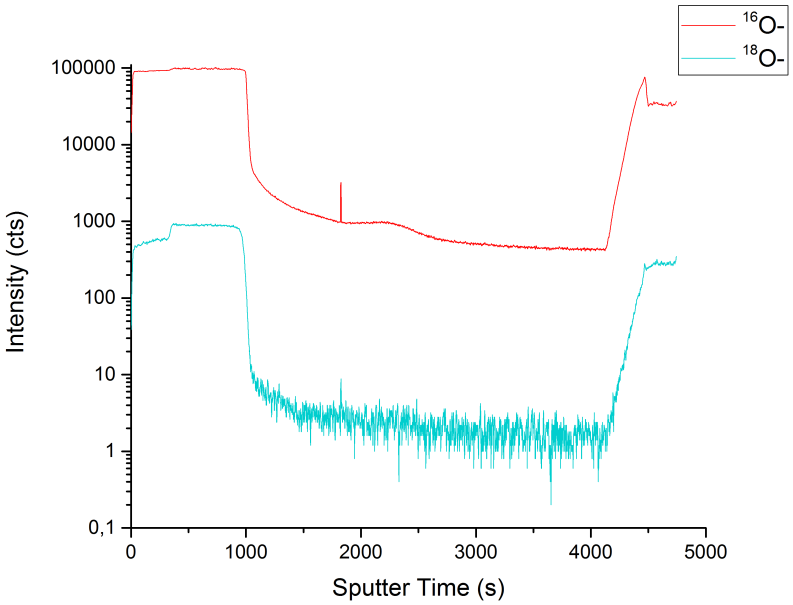

Figure 7.12: HfB_2 oxidised in synthetic air

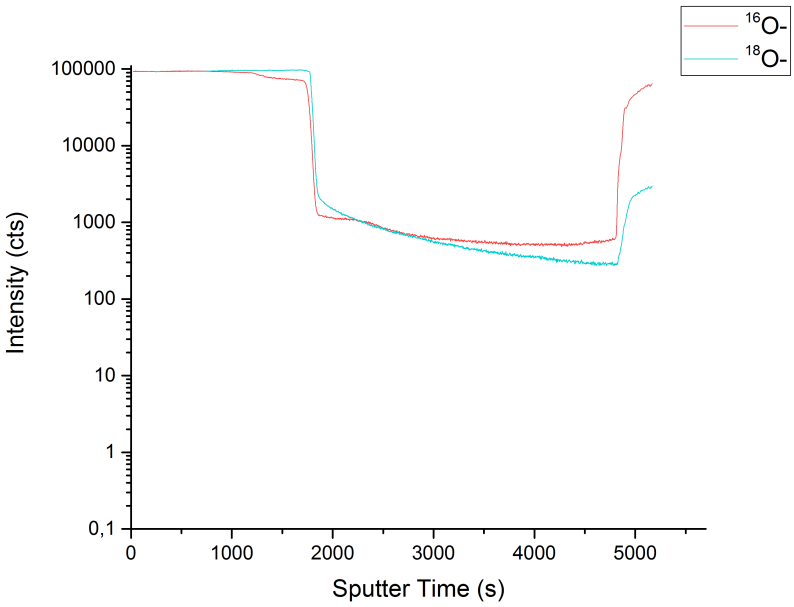

Figure 7.13: HfB_2 oxidised in an ^{18}O atmosphere

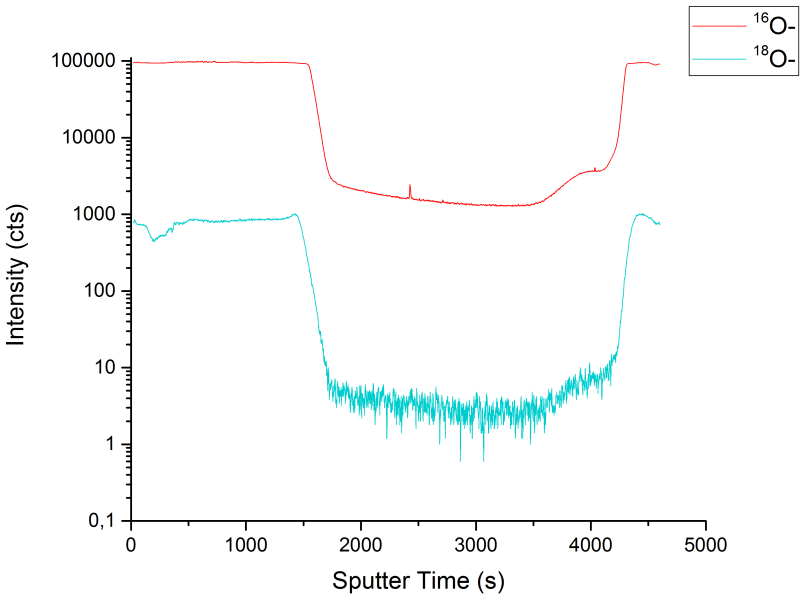

Figure 7.14: HfN oxidised in synthetic air

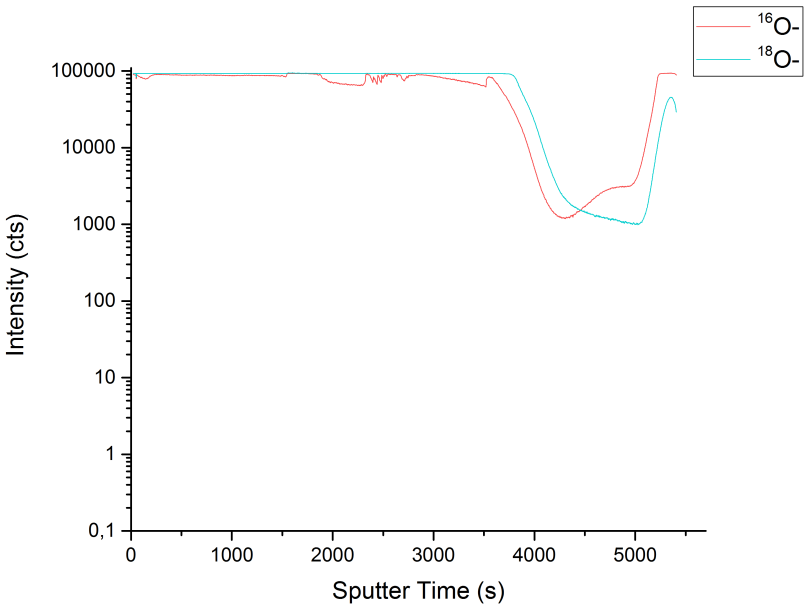

Figure 7.15: HfN oxidised in an ^{18}O atmosphere

7.2 SEM Measurements

SEM images of Hf, HfB_2 and HfN were obtained and analysed. Figure 7.16, 7.18 and 7.17 show the images obtained after the oxidation of Hf at 640 °C, of HfB_2 at 800 °C and of HfN at 840 °C.

Comparing the image of Hf with the images of the hafnium non-metal compounds a difference in the structure is recognisable. The thin films of the hafnium non-metal compounds are a lot denser than the Hf thin films as well as the oxide layer of the hafnium non-metal compounds are denser than the oxide layer of Hf. This could be a reason why more oxygen diffusion in Hf could be detected than in HfB_2 and HfN.

Comparing HfB_2 and HfN the intact layer of both materials look relatively similar, whereby HfB_2 seems to be a little denser than HfN. Looking at the oxide layer though the materials shows great differences.

Like already noticed with the ToF-SIMS depth profiles the oxide layer of HfB_2 consists of two different, almost equally thick layers. The crystalline-like structure is still discernible in the inner layer, which was assumed to be rich in hafnium and poor in boron, but the outer layer, which was assumed to be rich in boron and poor in hafnium, seems to be porous.

Looking at HfN also two oxide layers can be recognised, but the outer layer is a lot thinner than the inner layer, which has already been indicated by the ToF-SIMS depth profiles. The difference of both layers is not as clearly noticeable as the difference of the oxide layers of HfB_2, however looking at the left upper corner of the image, detaching of the upper layer is visible which clearly indicates the presence of two oxide layers.

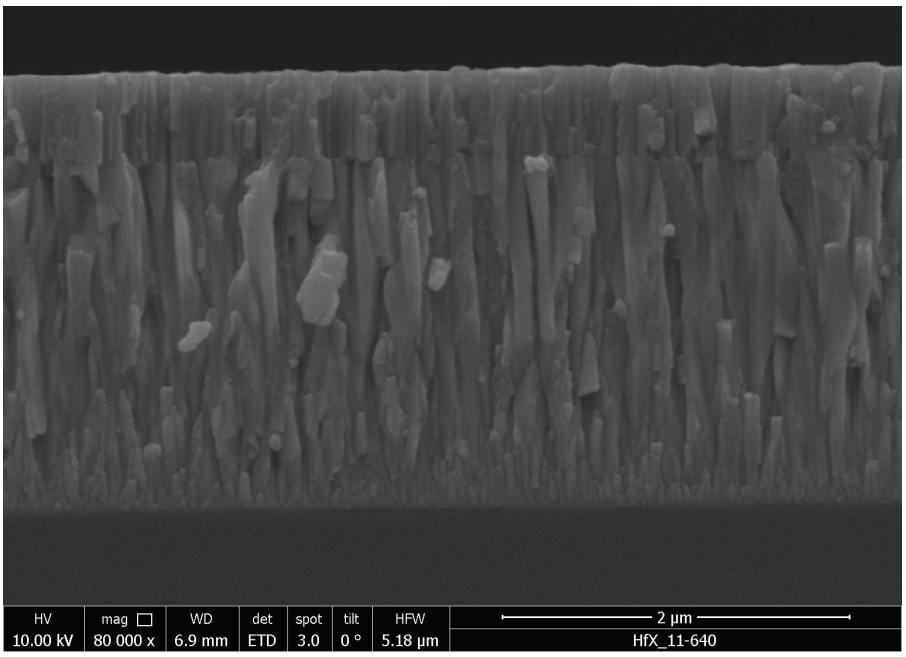

Figure 7.16: Hf oxidised at 640 °C for 1 h

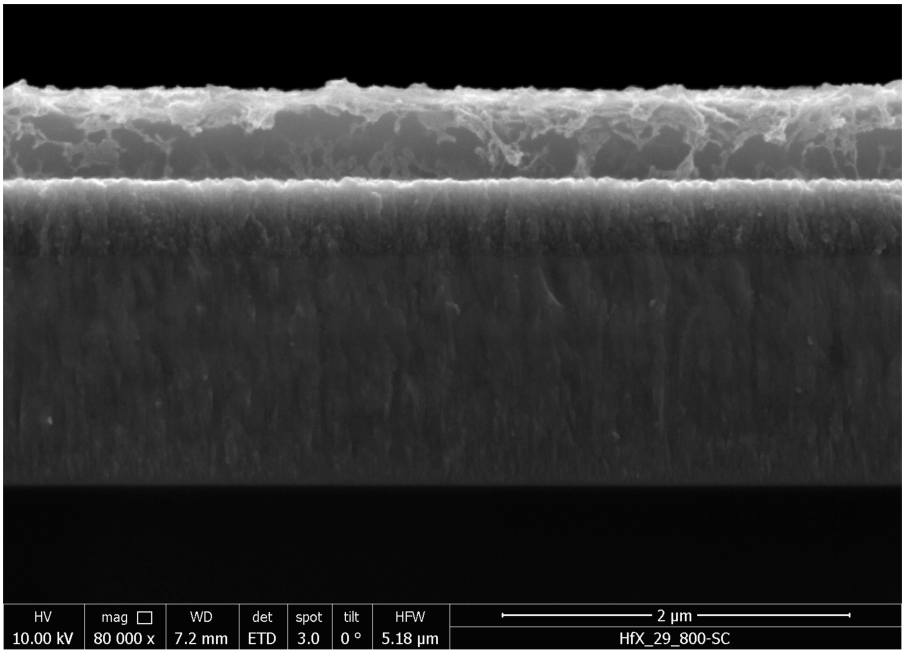

Figure 7.17: HfB_2 oxidised at 800 °C for 1 h

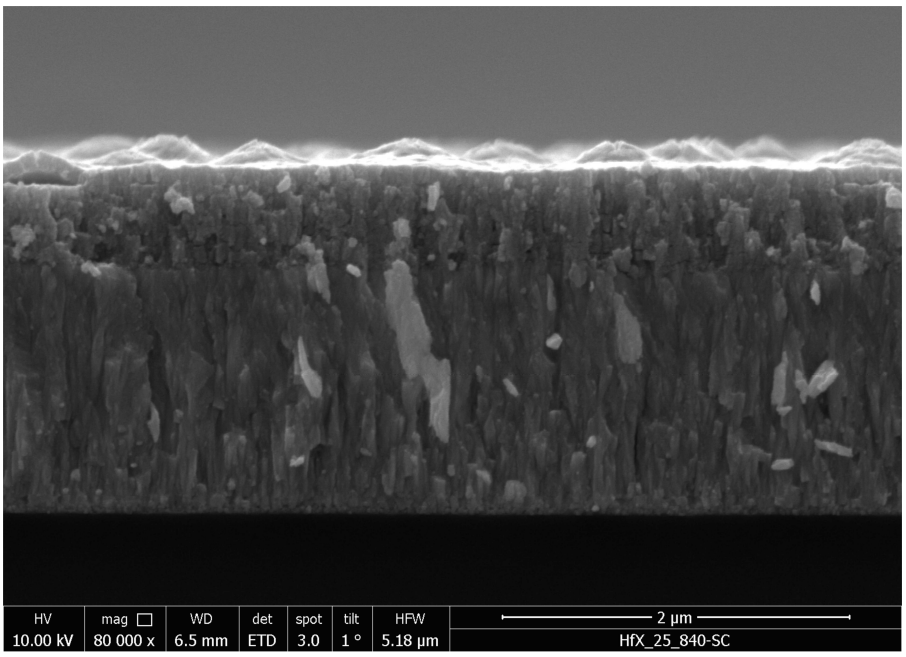

Figure 7.18: HfN oxidised at 840 °C for 1 h

The thickness of the oxide layers and of the intact material layer beneath of Hf, HfB_2 and HfN were determined and are shown in table 7.1.

The ratio between oxide layer and intact material layer determined with SEM images differs from the assumptions made on the basis of the ToF-SIMS depth profiles. This is not a surprise due to different sputtering speeds in different materials. When comparing the depth profiles of HfB_2 and HfN oxidised at 800 °C respectively 840 °C the oxide layer of the HfN samples seems to be a lot thicker than those of HfB_2. But comparing the actual thickness of the oxides determined with the SEM images it becomes clear that they are about the same, which indicates that HfB_2 is slower ablated than HfN.

Another cause for this effect could be that the thin films, used for the SEM images, were deposited onto SiC in contrast to the thin films analyst with the ToF-SIMS, which were deposited onto Sapphire. It is possible that the oxidation behaviour and with it the thickness of the oxide layer alters if the thin films are deposited

	Hf	HfB_2	HfN
Total thickness (μm)	2,519 ± 0.019	2,100 ± 0,002	2,017 ± 0,020
Total oxide layer (μm)	0.520 ± 0.018	0,715 ± 0,015	0,587 ± 0,043
Outer oxide layer (μm)		0,352 ± 0,022	0,107 ± 0,004
Inner oxide layer (μm)		0,372 ± 0,017	

Table 7.1: thickness of the oxide layer and the intact material layer beneath of Hf, HfB_2 and HfN

onto different substrates.

However, keeping in mind that the ratio between oxide layer and intact material layer could be influenced by different sputtering speed and looking again on the with ^{18}O treated HfB_2 and HfN thin films it is very likely that the ratio of oxide layer and intact material layer of both samples is also similar. Moreover it is likely that the oxide of the HfB_2 thin film is a lot thicker than assumed on the basis of the ToF-SIMS depth profiles and therefore the experiment should be repeated to obtain significant information of the oxygen diffusion into HfB_2 and HfN.

Moreover it would be of benefit to analyse the thin films deposited onto SiC also by generating depth profiles with a ToF-SIMS.

8 Conclusion

Hafnium based thin films, as potential candidates for protective aeroplane coatings, were analysed and it was determined that the non-metals in hafnium based thin films like HfB_2 and HfN have a big influence on the oxidation and oxygen diffusion behaviour when compared to the pure Hf thin films. Not only do the Hf thin films form an oxide layer at a significantly lower temperature than HfB_2 but also the oxygen diffusion is a lot higher in the Hf thin films at the onset temperature of the oxidation (640 °C) than the oxygen diffusion at the respective onset temperatures (800 °C respectively 840 °C) of HfB_2 and HfN.

Reheating the samples in an ^{18}O atmosphere the diffusion through the oxide layer into the intact material layer beneath was determined by analysing the $^{18}O^-$ intensity before and after the experiment. It was found that the oxide layers function as a protective layer but do not completely preserve the hafnium based thin films from oxygen diffusion.

Looking at the depth profiles of the oxidised thin films obtained with a ToF-SIMS and the images of cross sections of the oxidised thin films obtained with a SEM it becomes clear that HfB_2 and HfN form two different oxide layers, however those of HfB_2 alter both in structure and probably also in element composition.

Comparing HfB_2 and HfN, HfB_2 outperforms HfN in oxygen diffusion at higher temperatures (>900 °C). Nevertheless, both materials show great resistivity against temperature and oxidation making them very interesting for protective coating.

Bibliography

[1] B. Deal and A. Grove, "General relationship for the thermal oxidation of silicon," *Journal of Applied Physics*, vol. 36, no. 12, pp. 3770–3778, 1965.

[2] E. Wuchina, E. Opila, M. Opeka, W. Fahrenholtz, and I. Talmy, "Uhtcs: Ultra-high temperature ceramic materials for extreme environment applications," *Electrochemical Society Interface*, vol. 16, pp. 30–36, 2007.

[3] M. Opeka, I. Talmy, E. Wuchina, J. Zaykoski, and S. Causey, "Mechanical, thermal, and oxidation properties of refractory hafnium and zirconium compounds," *Journal of the European Ceramic Society*, vol. 19, no. 13, pp. 2405–2414, 1999.

[4] X. Zhang, X. Luo, J. Han, J. Li, and W. Han, "Electronic structure, elasticity and hardness of diborides of zirconium and hafnium: First principles calculations," *Computational Materials Science*, vol. 44, no. 2, pp. 411–421, 2008.

[5] D. T. E. Hayes, *The Metallurgy of Hafnium*. Washington: Government Printing Office, 1960, pp. 1–8.

[6] W. G. Fahrenholtz and G. Hilmas, "Ultra-high temperature ceramics: Materials for extreme environments," *Scripta Materialia*, vol. 129, pp. 94–99, 2017.

[7] C. Carter and M. Norton, *Ceramic Materials: Science and Engineering*. New York: Springer, 2013, p. 494.

[8] V. Matkovich, *Boron and Refractory Borides*. Berlin, Heidelberg: Springer, 1977, pp. 31–51.

[9] W. Hofmann and W. Jäniche, "Der strukturtyp von aluminiumborid (alb2)," *Naturwissenschaften*, vol. 23, no. 50, p. 851, 1935.

[10] W. Lipscomb and D. Britton, "Valence structure of the higher borides," *The Journal of Chemical Physics*, vol. 33, no. 1, pp. 275–280, 1960.

[11] T. Lunström, "Structure, defects and properties of some refractory borides," *Pure and Applied Chemistry*, vol. 57, no. 10, pp. 1383–1390, 1985.

[12] V. Matkovich, *Boron and Refractory Borides*. Berlin, Heidelberg: Springer, 1977, pp. 390–412.

[13] K. Ferber, P. Becher, and B. C. Finch, "Effect of microstructure on the properties of tib2 ceramics," *Journal of the American Ceramic Society*, vol. 66, no. 1, C-2-C–4, 1983.

[14] D. Sciti, L. Silvestroni, and A. Bellosi, "Fabrication and properties of hfb2–mosi2 composites produced by hot pressing and spark plasma sintering," *Journal of Materials Research*, vol. 21, no. 6, pp. 1460–1466, 2006.

[15] F. Monteverde, C. Melandri, and S. Guicciardi, "Microstructure and mechanical properties of an hfb2 +30vol% sic composite consolidated by spark plasma sintering," *Materials Chemistry and Physics*, vol. 100, no. 2, pp. 513–519, 2006.

[16] S. Jayaraman, J. Gerbi, Y. Yang, D. Kim, A. Chatterjee, P. Bellon, G. Girolami, J. Chevalier, and J. Abelson, "Hfb_2 and hf–b–n hard coatings by chemical vapor deposition," *Surface and Coatings Technology*, vol. 200, no. 22, pp. 6629–6633, 2006.

[17] W. Fahrenholtz, G. Hilmas, I. Talmy, and J. Zaykoski, "Refractory diborides of zirconium and hafnium," *Journal of the American Ceramic Society*, vol. 90, no. 5, pp. 1347–1364, 2007.

[18] H. Okamoto, "The hf-n (hafnium-nitrogen) system," *Bulletin of Alloy Phase Diagrams*, vol. 11, no. 2, pp. 146–149, 1990.

[19] C. Ribbing and A. Roos, *Handbook of Optical Constants of Solids*. Burlington: Academic Press, 1997, pp. 351–369.

[20] E. Wuchina, M. Opeka, S. Causey, K. Buesking, J. Spain, A. Cull, J. Routbort, and F. Guitierrez-Mora, "Designing for ultrahigh-temperature applications: The mechanical and thermal properties of hfb_2, hfc_x, hfn_x and alphahf(n)," *Journal of Materials Science*, vol. 39, no. 19, pp. 5939–5949, 2004.

[21] C. Escobar, M. Villarreal, J. C. Caicedo, J. Esteve, and P. Prieto, "Mechanical and tribological behavior of vn and hfn films deposited via reactive magnetron sputtering," *Surface Review and Letters*, vol. 20, no. 3and4, 1350040(1–12), 2013.

[22] E. T. Mitchell, "Mechanical properties of hafnium single crystals," *Metallurgical Transactions*, vol. 4, no. 5, pp. 1405–1413, 1973.

[23] I. Michelakaki, N. Boukos, D. Dragatogiannis, S. Stathopoulos, C. Charitidis, and D. Tsoukalas, "Synthesis of hafnium nanoparticles and hafnium nanoparticle films by gas condensation and energetic depositio," *Beilstein Journal of Nanotechnology*, vol. 9, pp. 1868–1880, 2018.

[24] M. McNallan and E. Opila, *High Temperature Corrosion and Materials Chemistry III*. New Jersey: The Electrocemical Society, 2001, pp. 136–144.

[25] W. Smeltzer and M. Simnad, "Oxidation of hafnium," *Acta Metallurgica*, vol. 5, no. 6, pp. 328–334, 1957.

[26] E. C. L. Kaufman and J. Berkowitz-Mattuck, "Oxidation characteristics of hafnium and zirconium diboride," *Transactions of the Metallurgical Society of AIME*, vol. 239, no. 4, pp. 458–466, 1967.

[27] J. Crank, *The Mathematics of Diffusion*, 2nd ed. Maidenhead: Cambridge University Press, 1979, pp. 1–10.

[28] H. Mehrer, *Diffusion in Solids: Fundamentals, Methods, Materials, Diffusion-Controlled Processes*. Berlin: Springer, 2007, p. 562.

[29] A. Benninghoven, "Chemical analysis of inorganic and organic surfaces and thin films by static time-of-flight secondary ion mass spectrometry (tof-sims)," *Angewandte Chemie International Edition in English*, vol. 33, no. 10, pp. 1023–1043, 1994.

[30] J. Vickerman and D. Briggs, *ToF-SIMS Surface Analysing by Mass Spectroscopy*. Huddersfield: IM Publications and SurfaceSpectra Limited, 2001, pp. 1–7.

[31] R. Behrisch, *Sputtering by Particle Bombardment I*. Berlin: Springer, 1981, pp. 145–218.

[32] J. Vickerman and D. Briggs, *ToF-SIMS Surface Analysing by Mass Spectroscopy*. Huddersfield: IM Publications and SurfaceSpectra Limited, 2001, pp. 95–120.

[33] S. Kayser. (2020). Latest developments in 2d and 3d tof-sims analysis, [Online]. Available: `https://www.ufz.de/export/data/2/152053_Latest%20Developments%20in%202D%20and%203D%20TOF-SIMS%20Analysis.pdf`.

[34] P. Sudraud, J. V. D. Walle, C. Colliex, and R. Castaing, "Contribution of field effects to the achievement of higher brightness ion sources," *Surface Science*, vol. 70, no. 1, pp. 392–402, 1978.

[35] M. Benguerba, A. Brunelle, S. Della-Negra, J. Depauw, H. Joret, Y. L. Beyec, M. Blain, E. Schweikert, G. Assayag, and P. Sudraud, "Impact of slow gold clusters on various solids: Nonlinear effects in secondary ion emission," *Nuclear Instruments and Methods in Physics Research Section B: Beam Interactions with Materials and Atoms*, vol. 62, no. 1, pp. 8–22, 1991.

[36] A. Brunelle, D. Touboul, and O. Laprévote, "Biological tissue imaging with time-of-flight secondary ion mass spectrometry and cluster ion sources," *Journal of Mass Spectrometry*, vol. 40, no. 8, pp. 985–999, 2005.

[37] S. Schwab, "Ion diffusion and migration in semiconductor passivation and encapsulation materials," PhD thesis, TU Vienna, 2017, pp. 1–7.

[38] B. Mamyrin, "Time-of-flight mass spectrometry (concepts, achievements, and prospects)," *International Journal of Mass Spectrometry*, vol. 206, no. 3, pp. 251–266, 2001.

[39] T. Bergmann, T. Martin, and H. Schaber, "High-resolution time-of-flight mass spectrometer," *Review of Scientific Instruments*, vol. 60, no. 4, pp. 792–793, 1989.

[40] C. Hunt, C. Stoddart, and M. Seah, "The surface analysis of insulators by sims: Charge neutralization and stabilization of the surface potential," *Surface and Interface Analysis*, vol. 3, no. 4, pp. 157–160, 1981.

[41] Y. Leng, *Materials Characterization: Introduction to Microscopic and Spectroscopic Methods*. Singapore: John Wiley and Sons, 2009, p. 238.

[42] M. Kubicek, G. Holzlechner, A. Opitz, S. Larisegger, H. Hutter, and J. Fleig, "A novel tof-sims operation mode for sub 100nm lateral resolution: Application and performance," *Applied Surface Science*, vol. 289, pp. 407–416, 2014.

[43] G. Holzlechner, M. Kubicek, H. Hutter, and J. Fleig, "A novel tof-sims operation mode for improved accuracy and lateral resolution of oxygen isotope measurements on oxides," *J. Anal. At. Spectrom.*, vol. 28, pp. 1080–1089, 7 2013.

[44] P. M. Martin, *Handbook of Deposition Technologies for Films and Coatings (Third Edition)*. Boston: William Andrew Publishing, 2010, pp. 253–296.

[45] A. Amsüss, "Diffusion and phase formation in the al-cu thin film system investigated with tof-sims and grazing incidence x-ray diffraction," PhD thesis, TU Vienna, 2018, p. 18.

[46] P. Hawkes and L. Reimer, *Scanning Electron Microscopy: Physics of Image Formation and Microanalysis*, ser. Springer Series in Optical Sciences. Berlin, Heidelberg, NewYork: Springer, 1998, pp. 1–20.

[47] L. S. snd D. Grubb and G. Meyers, *Polymer Microscopy*. NewYork: Springer, 2018, pp. 35–42.

[48] M. Baskaran, *Handbook of Environmental Isotope Geochemistry*, ser. Springer Series in Optical Sciences. Detroid: Springer, 2011, p. 438.

List of Figures

List of Tables